












## Accelerated Emergence of Evolved Galaxies in Early Overdensities at $z \sim 5.7$

TAKAHIRO MORISHITA <sup>1</sup>, ZHAORAN LIU <sup>2</sup>, MASSIMO STIAVELLI <sup>3,4,5</sup>, TOMMASO TREU <sup>6</sup>, MICHELE TRENTI <sup>7,8</sup>,  
NIMA CHARTAB <sup>1</sup>, GUIDO ROBERTS-BORSANI <sup>6,9</sup>, BENEDETTA VULCANI <sup>10</sup>, PIETRO BERGAMINI <sup>11,12</sup>,  
MARCO CASTELLANO <sup>13</sup> AND CLAUDIO GRILLO <sup>11,14</sup>

<sup>1</sup>*IPAC, California Institute of Technology, MC 314-6, 1200 E. California Boulevard, Pasadena, CA 91125, USA*

<sup>2</sup>*Astronomical Institute, Graduate School of Science, Tohoku University, 6-3 Aoba, Sendai 980-8578, Japan*

<sup>3</sup>*Space Telescope Science Institute, 3700 San Martin Drive, Baltimore, MD 21218, USA*

<sup>4</sup>*Dept. of Physics & Astronomy, Johns Hopkins University, Baltimore, MD 21218, USA*

<sup>5</sup>*Dept. of Astronomy, University of Maryland, College Park, MD 20742, USA*

<sup>6</sup>*Department of Physics and Astronomy, University of California, Los Angeles, 430 Portola Plaza, Los Angeles, CA 90095, USA*

<sup>7</sup>*School of Physics, University of Melbourne, Parkville 3010, VIC, Australia*

<sup>8</sup>*ARC Centre of Excellence for All Sky Astrophysics in 3 Dimensions (ASTRO 3D), Australia*

<sup>9</sup>*Department of Astronomy, University of Geneva, Chemin Pegasi 51, 1290 Versoix, Switzerland*

<sup>10</sup>*INAF Osservatorio Astronomico di Padova, vicolo dell'Osservatorio 5, 35122 Padova, Italy*

<sup>11</sup>*Dipartimento di Fisica, Università degli Studi di Milano, Via Celoria 16, I-20133 Milano, Italy*

<sup>12</sup>*INAF - OAS, Osservatorio di Astrofisica e Scienza dello Spazio di Bologna, via Gobetti 93/3, I-40129 Bologna, Italy*

<sup>13</sup>*INAF Osservatorio Astronomico di Roma, Via Frascati 33, 00078 Monteporzio Catone, Rome, Italy*

<sup>14</sup>*INAF - IASF Milano, via A. Corti 12, I-20133 Milano, Italy*

(Received August 21, 2024)

Submitted to ApJ

### ABSTRACT

We report the identification of two galaxy overdensities at  $z \sim 5.7$  in the sightline of the galaxy cluster Abell 2744. These overdensities consist of 25 and 17 member galaxies, spectroscopically confirmed with JWST NIRSpec/MSA and NIRCам/WFSS. Each overdensity has a total stellar mass of  $\sim 2 \times 10^{10} M_{\odot}$  and a star formation rate of  $\sim 200 M_{\odot}/\text{yr}$  within a central region of radius  $R = 2 \text{ Mpc}$  (physical). The sensitive PRISM spectra allow us to identify six galaxies that show weak  $\text{H}\alpha + [\text{N II}]$  emissions within the overdensities ( $27 \pm 6\%$ ), whereas the fraction of such galaxies is found significantly lower ( $6 \pm 2\%$ ) in field samples of the equivalent redshift range. These weak emission line galaxies, dubbed as wELGs, exhibit a strong continuum break at  $4000 \text{ \AA}$  rest-frame, a characteristic feature of evolved stellar populations. The high observed fraction of wELGs in the two overdensities is consistent with the idea that high-density environments are an ideal site where galaxies can accelerate their evolutionary pace compared to field analogs. Our study pinpoints an early onset of environmental effects, already important within one billion years after the Big Bang, and provides a complementary perspective on the emergence of quenched, massive galaxies at lower redshifts. Potential contributions from black hole accretion feedback to the reduction of star formation activity are discussed, but the connection to the local environments remains unclear.

### 1. INTRODUCTION

Early galaxy overdensities mark unique spots in the universe and play critical roles in hierarchical structural formation. Starting in initial matter density peaks, by

bringing together dark matter and gas flows, they allow galaxies to efficiently form and evolve. Over time, interactions among surrounding galaxies and gaseous media further enhance star formation and chemical enrichment, leading to the maturation of galaxies within these gravitationally bounded systems. Such unique environments culminate in the distinctive features of cluster galaxy populations seen in the local universe: clus-

ters and groups are occupied by quiescent, dispersion-dominated, massive galaxies, whereas the fraction of younger, fast-rotating, actively star-forming galaxies inversely correlates with the local density (e.g., Dressler 1980; Thomas et al. 2005; Cappellari et al. 2011).

When, where, and how such distinct features began to appear has been a central question. Observational studies have extended the redshift frontier beyond the local universe, successfully capturing the transition of cluster galaxy properties over a wide range of cosmic time, indicative of environmental processes at work (e.g., Dressler et al. 1997; Treu et al. 2003; Steidel et al. 2005; Kodama et al. 2007; Newman et al. 2015; Wang et al. 2016). The frontier now extends to  $z > 3$ , where a substantial number of (proto-) clusters and overdensities have been identified from large surveys (e.g., Steidel et al. 2000; Capak et al. 2011; Casey 2016; Lemaux et al. 2018; Higuchi et al. 2019; Toshikawa et al. 2024), and even reaches the first billion years of cosmic history (Castellano et al. 2018, 2023; Harikane et al. 2019; Hu et al. 2021; Laporte et al. 2022; Morishita et al. 2023; Sun et al. 2023; Herard-Demanche et al. 2023; Helton et al. 2024).

Recent studies found massive galaxies that reside in overdensities out to  $z \sim 5$  (Tanaka et al. 2024; Kakiimoto et al. 2024; de Graaff et al. 2024; Jin et al. 2024; Alberts et al. 2023). Intriguingly, many of these massive galaxies show little or no ongoing star formation, suggesting that the overdensities act as accelerated environments for galaxy evolution. Even at higher redshifts, a study has shown that JADES-GS-z7-01-QU, a galaxy at  $z = 7.3$  (Looser et al. 2023), is located in an excess of strong line emitters (Helton et al. 2023, also Daikuhara, in prep.).

However, the presence of quiescent galaxy populations in early overdensities is puzzling. It even seems to contradict with the expectations of large gas reservoirs (e.g., Cai et al. 2017; D’Amato et al. 2020; Umehata et al. 2021) and with the fact that galaxies are generally experiencing elevated levels of star formation therein (e.g., Elbaz et al. 2007; Cooper et al. 2008; Hayashi et al. 2016; Shimakawa et al. 2018; Pérez-Martínez et al. 2024; Laishram et al. 2024).

Furthermore, the well-established environmental quenching (e.g., Peng et al. 2010; Wetzel et al. 2012), where galaxies are quenched through physical mechanisms such as ram-pressure/tidal stripping and interactions after infall, is not expected to be the dominant channel for star formation quenching at such early times (e.g., Dannerbauer et al. 2017). If the ubiquity of quiescent galaxies in early overdensities is indeed confirmed, it suggests the need for quenching processes that pref-

erentially operate in such environments. Otherwise, the origin may be attributed to self-driven processes, such as feedback from supernovae and active galactic nuclei (AGN). The current sample size of high- $z$  overdensities is small, preventing us from reaching robust conclusions.

In this paper, we report the discovery of two galaxy overdensities at  $z \sim 5.7$  in the sightline of the galaxy cluster Abell 2744. Spectroscopic data from multiple JWST programs identify 42 member galaxies within these overdensities. The sensitive spectrographs onboard JWST enable us to measure their star formation activity through rest-frame optical emission lines and to infer their formation history from the underlying stellar populations. Remarkably, we observe a significant excess of galaxies with reduced star formation in both overdensities – compared to the surrounding field – suggesting that galaxy evolution is already influenced by these environments. By exploiting these systems as a laboratory, our study aims to provide a unique perspective on initial assembly and growth of galaxies in early overdensities, and the quenching processes therein.

This paper is structured as follows: In Sec. 2, we present the dataset used and the details of reduction. In Sec. 3, we report the discovery of the two overdensities and their large-scale characterization. In Sec. 4, we investigate physical properties of a subset of the spectroscopic samples and report the population of weak emission line galaxies, which carries a critical role in this paper. In Sec. 5, we discuss the physical origin of the reduced star formation activities and their prevalence in the overdensities. In Sec. 6, we provide the summary. Where relevant, we adopt the AB magnitude system (Oke & Gunn 1983; Fukugita et al. 1996), cosmological parameters of  $\Omega_m = 0.3$ ,  $\Omega_\Lambda = 0.7$ ,  $H_0 = 70 \text{ km s}^{-1} \text{ Mpc}^{-1}$ , and the Chabrier (2003) initial mass function.

## 2. DATA

We briefly describe our JWST/NIRCam and NIRSpec data to be used in this work. Our target field in this paper is in the sightline of Abell 2744 (hereafter A2744), a massive cluster of galaxies at  $z = 0.308$  (00:14:18.9, -30:23:22).

### 2.1. JWST/NIRCam Imaging

The field has a wealth of NIRCam data sets taken in multiple programs in Cycles 1 and 2, including GLASS-JWST (ERS1324; Treu et al. 2022), UNCOVER (GO2561; Bezanson et al. 2022), DD2756 (Chen et al. 2022), GO2883 (PI F. Sun), GO3516 (PI J. Matthee), GO3538 (PI E. Iani), BEACON (GO3990; Morishita, in prep.), and Medium Bands, Mega Science (GO4111;

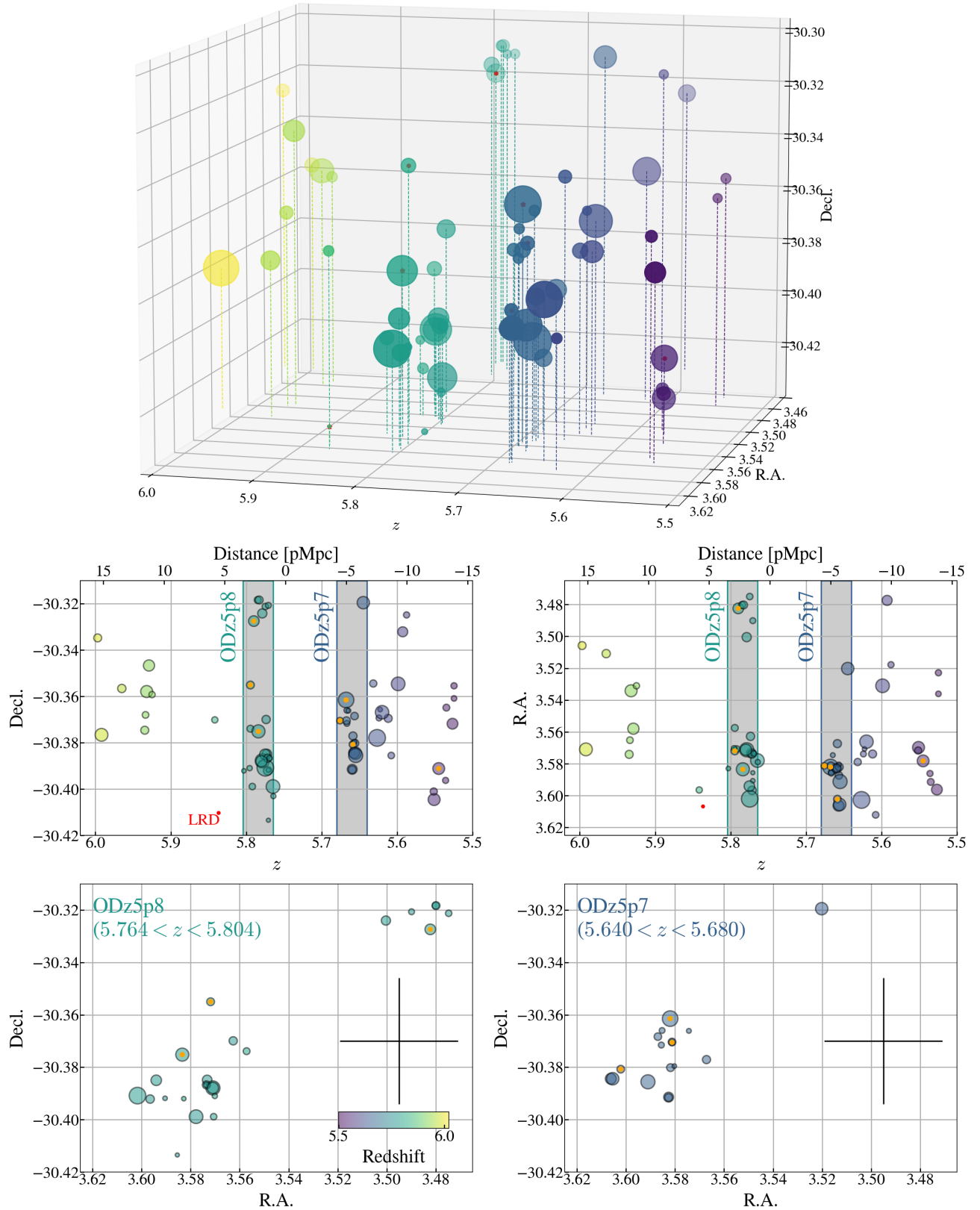


**Figure 1.** Distribution of spectroscopically confirmed galaxies at  $5.5 < z < 6.0$  in the Abell2744 field, in a three-dimensional space (top) and two-dimensional planes (bottom four panels). Two overdense regions are identified at  $z = 5.68$  (ODz5p8) and  $5.78$  (ODz5p7). The data points are color-coded by redshift and scaled by stellar mass. The galaxies showing weak  $H\alpha + [N II]$  emissions are identified (Sec 4.1) and marked separately (orange hexagons). Note that lens magnification has been corrected and the sources are shown in their source plane coordinates. Scale bars for  $\sim 1$  pMpc are shown in the bottom two panels. The isolated red point at  $z = 5.84$  is a “Little Red Dot” (Sec. 3).

Suess et al. 2024). We follow the same steps for JWST/NIRCam imaging reduction and photometry as presented by Morishita & Stiavelli (2023). Briefly, we retrieved the level1 (`uncal.fits`) NIRCam imaging data from MAST and processed with the official JWST pipeline<sup>1</sup>. The reduction process includes extra steps to minimize artifacts, such as extra snow ball masking and  $1/f$ -noise subtraction. The images are then combined in each filter and aligned to a reference image, here we use the publicly available image produced by the GLASS-JWST team (Merlin et al. 2022; Paris et al. 2023). The final images are then resampled to the same pixel grid of the pixel size of  $0.''0315$ . We utilize the HST ACS and WFC3-IR mosaic images publicly available by the GLASS-JWST team, which combined data from multiple HST programs (Postman et al. 2012; Lotz et al. 2017; Kelly et al. 2018; Steinhardt et al. 2020).

We identified sources in the IR detection image (F277W+F356W+F444W stack) using SExtractor (Bertin & Arnouts 1996), and measured fluxes on the psf-matched mosaic images with a fixed aperture of radius  $r = 0.''16$ . The PSF-matched fluxes are calibrated using the method introduced in Morishita & Stiavelli (2023). The magnification by the foreground cluster is corrected for each source by using the latest magnification model by Bergamini et al. (2023a,b).

In addition to previously confirmed spectroscopic sources (details in Sec. 2.2), we identify candidate galaxies at  $z \sim 5.7$  to be inspected in our NIRCam WFSS analysis in Sec. 2.3. For this, we preselect sources by the Lyman-break dropout method (Steidel et al. 1998), followed by a stringent photometric redshift selection, as was adopted in previous studies (Morishita et al. 2024). We apply the following selection cut:

$$\begin{aligned} S/N_{F444W} &> 5 \\ S/N_{<1216} &< 3 \\ 5.4 < z_{\text{phot}} &< 6.2, \end{aligned}$$

where the blue filters (rest-frame wavelength of  $< 1216 \text{ \AA}$  i.e. F070W and bluer) are used for non-detection, and  $z_{\text{phot}}$  is the peak redshift obtained with phot-z code `eazy` (Brammer et al. 2008).

We utilize the JWST+HST photometric data to infer the spectral energy distribution (SED) of spectroscopically confirmed galaxies, by using SED fitting code `gsf` (ver1.85; Morishita et al. 2019). The SED-based star-formation rate is calculated with the rest-frame UV luminosity ( $\sim 1600 \text{ \AA}$ ) using the `gsf`-determined SED

model. The UV luminosity is then corrected for the inferred dust attenuation. The attenuation corrected UV luminosity is converted to SFR via the relation by Kennicutt (1998):

$$\text{SFR} [M_{\odot} \text{ yr}^{-1}] = 1.4 \times 10^{-28} L_{\text{UV}} [\text{erg s}^{-1} \text{ Hz}^{-1}]. \quad (1)$$

The estimated SFR is then corrected for the Chabrier IMF, by multiplying by a factor of 0.63 (Madau & Dickinson 2014). The measured properties from the SED analysis are summarized in Table 1.

## 2.2. JWST/NIRSpec MSA

We utilize the spectroscopic catalog presented by Roberts-Borsani et al. (2024). The work processed publicly available JWST/NIRSpec Micro-Shutter Assembly (MSA) PRISM spectroscopic data in multiple fields. Spectroscopic redshift measurements were compiled after identification of bright optical emission lines, such as [O III] and H $\alpha$ , and visual inspection for any flagging sources. Readers are referred to the original work for the full detail of the reduction and analysis. The catalog consists of 167 sources at  $z > 5$  in the A2744 field, collected from three observing programs, GO2561, DDT2756, and GO3073 (Castellano et al. 2024).

For the line flux measurements, we fit each bright line with a Gaussian model. The lines close in wavelength (i.e. H $\beta$ + [O III] doublets, H $\alpha$ + [N II] doublets) are fitted simultaneously. The flux continuum is estimated by fitting a second-order polynomial over the non-line wavelength range defined for each targeted line and is subtracted before the line fit. The flux contribution from the absorption of Balmer lines is corrected by using the best-fit stellar template (without emission line component) derived by the aforementioned SED modeling.

## 2.3. JWST/NIRCam WFSS

Unlike NIRSpec-MSA, WFSS offers unbiased identification of strong emitters without requiring pre-selection of sources. We utilize two NIRCam-WFSS spectroscopic programs that are configured with the NIRCam F356W or F335M filters (GO3516 and GO3538), which offer the wavelength coverage for H $\beta$ + [O III] lines at the redshift range of our interest.

We follow a similar reduction process as Liu et al. (2024), which is motivated by the median filter technique introduced in Kashino et al. (2023). The reduction adopts ‘‘line scanning’’ after subtracting continuum fluxes over the wavelength range of interest for each target. This process involves a combination of the official JWST pipeline and several customized steps, as detailed below. We start by obtaining the stage-1 products (`rate.fits`) from the MAST archive. We then assign

<sup>1</sup> <https://github.com/spacetelescope/jwst>



the world coordinate system (WCS) and perform flat fielding on each frame using the most recent data available from the JWST Calibration Reference Data System (CRDS). Our background subtraction process consists of two steps. First, we subtract a median background created separately for each module and pupil. To further improve data quality and remove any remaining background, we use **SExtractor** (Bertin & Arnouts 1996) for additional subtraction. We then extract the emission line by removing the continuum, which is modeled using a median filter method with a smoothing kernel. With the background and continuum subtracted images, we are able to search for  $H\beta+[O\ III]$  emission lines in photometrically selected galaxies (Sec. 2.1) by locating the 2D spectra along the dispersion direction, using the spectral tracing and grism dispersion models generated by Sun et al. (2023).

Given the small wavelength range of extracted spectra, and potential contamination by other sources at a similar position in the cross-dispersion direction, we only include sources that have the pair of  $H\beta+[O\ III]$  doublet lines. This means that those with a single line cannot unambiguously be determined its redshift.

### 3. DISCOVERY OF TWO OVERDENSITIES OF GALAXIES AT $Z \sim 5.7$

Figure 1 shows the distribution of spectroscopically confirmed sources at  $5.5 < z < 6.0$  in the A2744 field. Remarkably, we find two concentrations of galaxies at  $z \sim 5.66$  and  $z \sim 5.78$ . By taking a redshift window of  $\Delta_z = 0.04$ , which corresponds to  $\sim 2$  pMpc (similar to the probed projected area), the two overdensities consist of 17 and 25 member galaxies, respectively. Despite being in the same sightline, the physical separation of the two overdensities is  $\sim 6$  pMpc along the redshift space. As such, in what follows we proceed our analyses by treating the two overdensities as isolated from each other, rather than as a single large-scale structure. We hereafter refer to these overdensities as ODz5p7 ( $5.640 < z < 5.680$ ) and ODz5p8 ( $5.764 < z < 5.804$ ). For the sake of simplicity, we refer to the remaining sources as “field” samples ( $N = 29$ ).

Most of the member galaxies are concentrated within the area of projected  $R \sim 0.5$  pMpc. There are a few galaxies at a further distance,  $\sim 3$  pMpc from the primary concentration. We note, however, that the empty region between the primary and the secondary concentrations is likely, if not completely, due to the lack of WFSS coverage (Fig. 2). As such, mass and star formation rate measurements of the overdensities themselves in what follows likely serve as lower limits.

We estimate overdensity,  $\delta = (n - \bar{n})/\bar{n}$ , which represents the excess of surface number density from the field average, by following the same procedure as in Morishita et al. (2023). In each overdensity, we use  $R = 0.5$  pMpc and the redshift range as defined above. For the field reference, we use the luminosity function at  $z \sim 6$  presented in Bouwens et al. (2021) and integrated it down to  $M_{UV} \sim -18$  mag, approximately the lower  $1\sigma$  from the mean observed  $M_{UV}$  in each concentration. For the area within  $R = 0.5$  pMpc from the peak density, we measure  $\delta = 3.4^{+3.7}_{-1.2}$  and  $6.9^{+9.3}_{-2.5}$  for ODz5p7 and ODz5p8, respectively, where the quoted uncertainty is Poisson noise.

Figure 3 shows the redshift distributions of galaxy counts, the total stellar mass, and the total star formation rate in each redshift bin. Despite the larger number of galaxies in ODz5p8, both overdensities have similar total stellar masses ( $\sim 2 \times 10^{10} M_\odot$ ) and total star formation rates ( $\sim 200 M_\odot \text{yr}^{-1}$ ).

The halo mass at the time of the observed redshift is estimated by integrating the halo mass of individual member galaxies, where the individual halo mass is calculated by the empirical  $M_h - M_{UV}$  relation at  $z \sim 6$  in Mason et al. (2022). We estimate it to be  $\log M_h/M_\odot \approx 12.0$  and  $\approx 12.2$  for ODz5p7 and ODz5p8, respectively. Instead, when the empirical  $M_h - M_*$  relation at  $z \sim 6$  in Behroozi et al. (2019) is adopted, we obtain  $\log M_h/M_\odot \approx 12.4$  and  $\approx 12.6$ . The increased halo mass by the latter method is likely due to the fact that our galaxies are not very young, which is instead assumed for the  $M_h - M_{UV}$  relation, leading to a reduced  $M_h$  value for a given  $M_{UV}$ .

Both the estimated  $\delta$  and the halo masses suggest that each overdensity is expected to evolve into a system of  $\gtrsim 10^{14} M_\odot$  by  $z \approx 0$  (see e.g. Fig. 5 in Toshikawa et al. 2014). Figure 4 shows the halo masses of the two overdensities along with measurements in the literature. Predicting the mass of a descendant system generally involves uncertainties, especially when the field of view (FoV) is limited (see Sec. 4.2 of Morishita et al. 2023). Nevertheless, comparisons with mass growth trajectories from simulations (Lim et al. 2024) suggest that these two overdensities would have evolved into massive systems by  $z \sim 0$ .

We find no excess of Ly $\alpha$  emitters in either of the overdensities. We find one Ly $\alpha$  emitter within ODz5p8 (of 16 having the wavelength coverage) and none within ODz5p7 (of 9), whereas two are found in the field sample (of 24).

Lastly, one of the spectroscopically confirmed sources, ID43506 at  $z = 5.84$ , exhibits a v-shape spectrum, a characteristic feature of the recently discovered “Little Red Dot” population (e.g., Furtak et al. 2023; Matthee

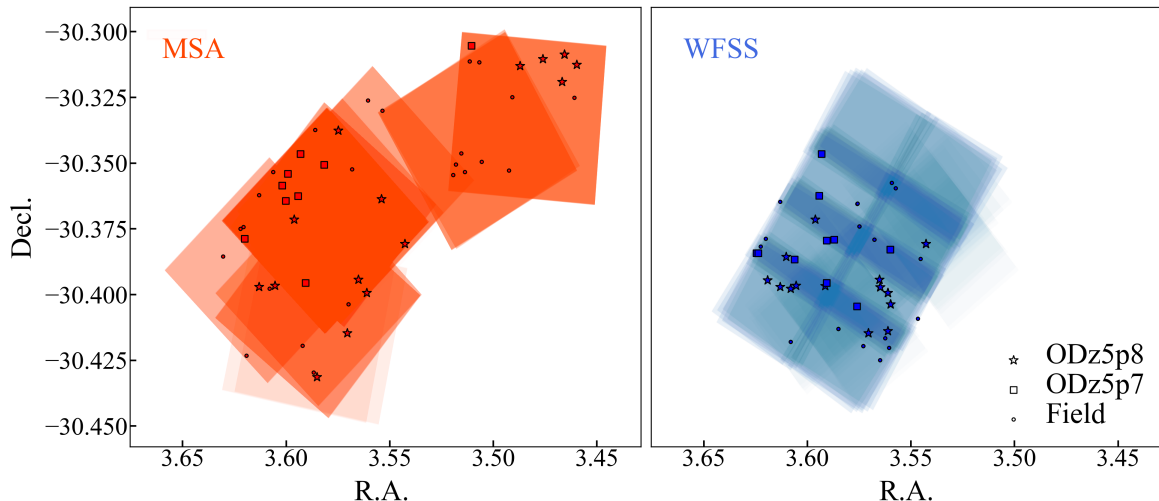


**Figure 2.** Spectroscopic data coverage (MSA in the left panel and WFSS in right). Spectroscopically confirmed sources by the corresponding instrument are shown in each of the panels. The color transparency represents the total exposure time. Note that the sources are shown in the observed sky positions, whereas Fig. 1 shows their source-plane positions after correcting for lens magnification.

et al. 2023; Greene et al. 2024). Additionally, the spectrum shows line broadening in  $H\alpha$  and  $H\beta$ , suggesting the presence of an AGN. This source is isolated from other galaxies in the field (Fig. 1). We found that the estimated stellar mass and star formation rate for this source are uncertain, as the observed fluxes could be dominated by AGN. As such, we exclude this source in the following analysis.

#### 4. SPECTROSCOPIC PROPERTIES OF MEMBER GALAXIES

The sensitivity and wavelength coverage of NIRSpec MSA spectra allow us not only to confirm spectroscopic members, but also investigate the physical properties of individual galaxies. In this section, we focus on the MSA samples for further characterization of their properties. For simplicity, hereafter we refer to galaxies in one of the two overdensities as overdensity samples, and others as field samples.

##### 4.1. $H\alpha + [N II]$ Emission Line Equivalent Width

For the redshift range of the two overdensities,  $H\alpha + [N II]$  emissions lines fall within the spectral range of NIRSpec PRISM. The spectral resolution at the relevant wavelength ( $\sim 4.4 \mu\text{m}$ ) is  $R \sim 200$ , which barely resolves the  $H\alpha$  from the  $[N II]$  doublets. As such, while we fit the line complex with a three-component Gaussian model (Sec. 2.2), we only use the integrated flux of the three lines in the following discussion. Among the NIRSpec MSA sample, we could obtain a reliable EW measurement in 40 galaxies. We note that the WFSS samples are not covered with their  $H\alpha$  or  $[N II]$  lines, and thus they are excluded from the discussion below.

The measured rest-frame equivalent widths,  $EW_0(H\alpha + [N II])$ , are shown in Fig. 5. For those with the underlying continuum undetected or uncertain, we quote a lower limit by using the RMS of the spectrum in the relevant wavelength range. For those with the continuum detected but emission lines undetected, we quote an upper limit.

The majority of the sample galaxies range between  $\sim 200$  and  $2000 \text{ \AA}$ , with a median value of  $\sim 300 \text{ \AA}$ , which is consistent with the measurements at similar redshifts by Roberts-Borsani et al. (2024). Among those, we find nine galaxies showing a significantly reduced value,  $\lesssim 100 \text{ \AA}$ , which we hereafter refer to as weak emission line galaxies, or wELGs. The identified wELGs are relatively high mass ( $\log M_*/M_\odot \gtrsim 8.4$ ) compared to the entire distribution.

Remarkably, all except one wELGs are found within one of the two discovered overdensities. Among the MSA samples, the fraction of wELGs in the overdensities is 3/8 (ODz5p7) and 3/14 (ODz5p8), whereas it is much smaller in the field sample (1/17). It is noted that the dominance of wELGs in the overdensities is unlikely due to the selection effect. While the WFSS samples are not included in the statistics, adding those as non-wELGs would give fractions of 3/15, 3/23, and 1/26, for ODz5p7, ODz5p8, and the field sample, respectively.

In addition, we investigate the fraction of wELGs in other fields of Roberts-Borsani et al. (2024). Among 141 sources at  $5.5 < z < 6.0$  that are successfully fitted, we find eight sources that satisfy  $EW_0(H\alpha + [N II]) < 100 \text{ \AA}$ , which gives a similar ratio of wELGs to our field sample. This confirms that the field sample defined in this study

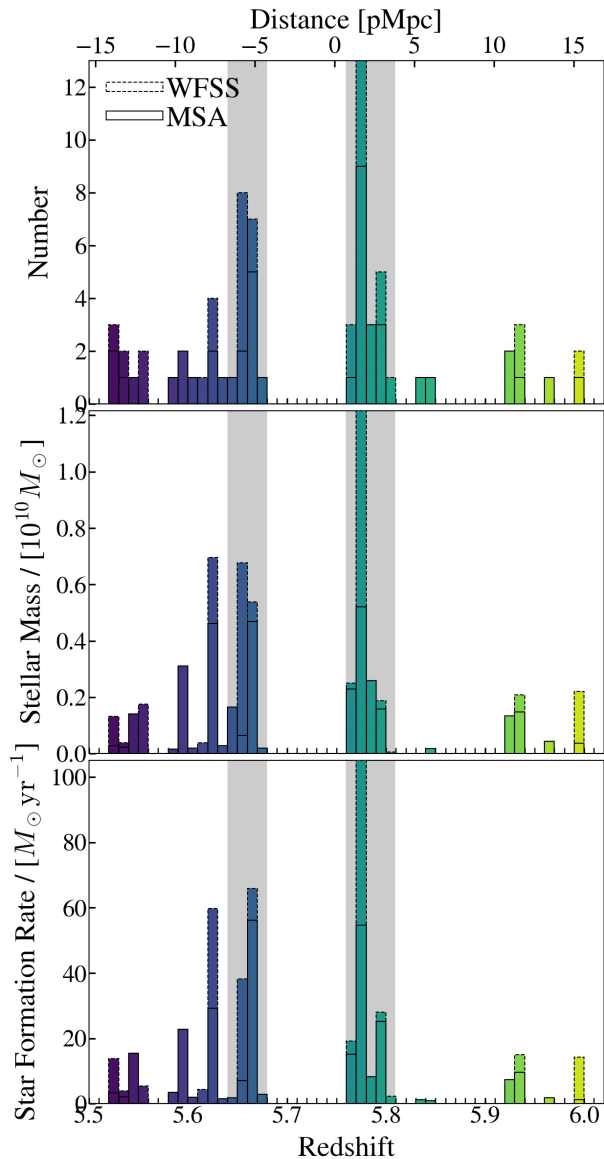


**Figure 3.** Redshift distributions of the spectroscopically confirmed galaxies in the sightline of A2744 (top). The weighted distributions by stellar mass (middle) and by star formation rate (bottom) are also shown. Solid lines are for the MSA sample and dashed lines for the WFSS sample. The redshift ranges of the two overdensities are hatched in gray.

does not significantly differ from representative samples at the same redshift.

From the comparison of the fractions of wELGs in the two field samples, it is suggested that wELGs are more ubiquitous in overdensities. In fact, the only wELG in the field sample (ID52153) is located in a less pronounced overdensity, a concentration of four galaxies, which further supports the hypothesis.

We find a larger scatter observed in the  $EW_0(\text{H}\alpha + [\text{N II}])$  measurements of the overdensity samples than

the field samples (Fig. 5). Not only wELGs, the overdensity sample consists of a few emitters at the *high* EW end ( $\gtrsim 1000 \text{ \AA}$ ) too. This suggests that the star formation activity of galaxies in overdensities is likely less constrained than in the field sample, implying the presence of physical processes that are more common in the former environment. We revisit this in Sec. 5.

#### 4.2. Strength of the $4000 \text{ \AA}$ +Balmer Break

The spectrum of one of the identified wELGs is shown in Fig. 6. Besides the modest star formation activity measured in their emission lines, we find that wELGs generally show a pronounced continuum break at rest-frame  $4000 \text{ \AA}$ , a characteristic features of evolved galaxies after having a short starburst (Dressler & Gunn 1983; Dressler et al. 1999). Such a characteristic break is not seen in the majority of sources at similar redshifts. In Fig. 6, we show the composite spectrum of  $z \sim 5.5$  galaxies presented in Roberts-Borsani et al. (2024) for comparison. Beside the pronounced continuum break, this example wELG shows a redder UV slope. From these differences in the two spectra, it is suggested that wELGs are distinct from the representative galaxies at similar redshift.

To quantify the difference, we measure the strength of the continuum break by taking the ratio of mean flux density in both red and blue sides,  $D_e4000 = f_{\nu,4250}/f_{\nu,3350}$ <sup>2</sup>. The average flux densities are measured in  $f_{\nu}$ , over the rest-frame wavelength range of  $3050 < \lambda/\text{\AA} < 3650$  and  $3950 < \lambda/\text{\AA} < 4550$ , respectively, effectively capturing both Balmer and  $4000 \text{ \AA}$  breaks. The wavelengths of any emission lines, such as  $\text{H}\gamma$  and  $\text{H}\delta$ , are masked out from the continuum flux estimate.

The  $D_e4000$  index can be securely measured upon the significant detection of continuum fluxes in both wavelength windows. Among 49 MSA sample, we could successfully measure the strength for 30 galaxies within the uncertainty of  $< 0.1$  dex. Fig. 7 shows the distribution of those break measurements as a function of light-weighted age derived from our SED analysis.

We find that wELGs have systematically stronger Balmer break than the non-wELG samples. This is partially due to the lack of sources of  $\log t/\text{Gyr} \lesssim 1.6$  in the wELG samples, the regime which is dominated by young, strong emission line galaxies. More importantly, for a given age wELGs exhibit a relatively stronger break than non-wELGs. Also shown in Fig. 7 is a theoretical

<sup>2</sup> The subscript, *e*, represents “extended,” to distinguish from the conventional  $D4000$  (or  $D_n4000$ ) index, which is defined within narrower wavelength ranges.

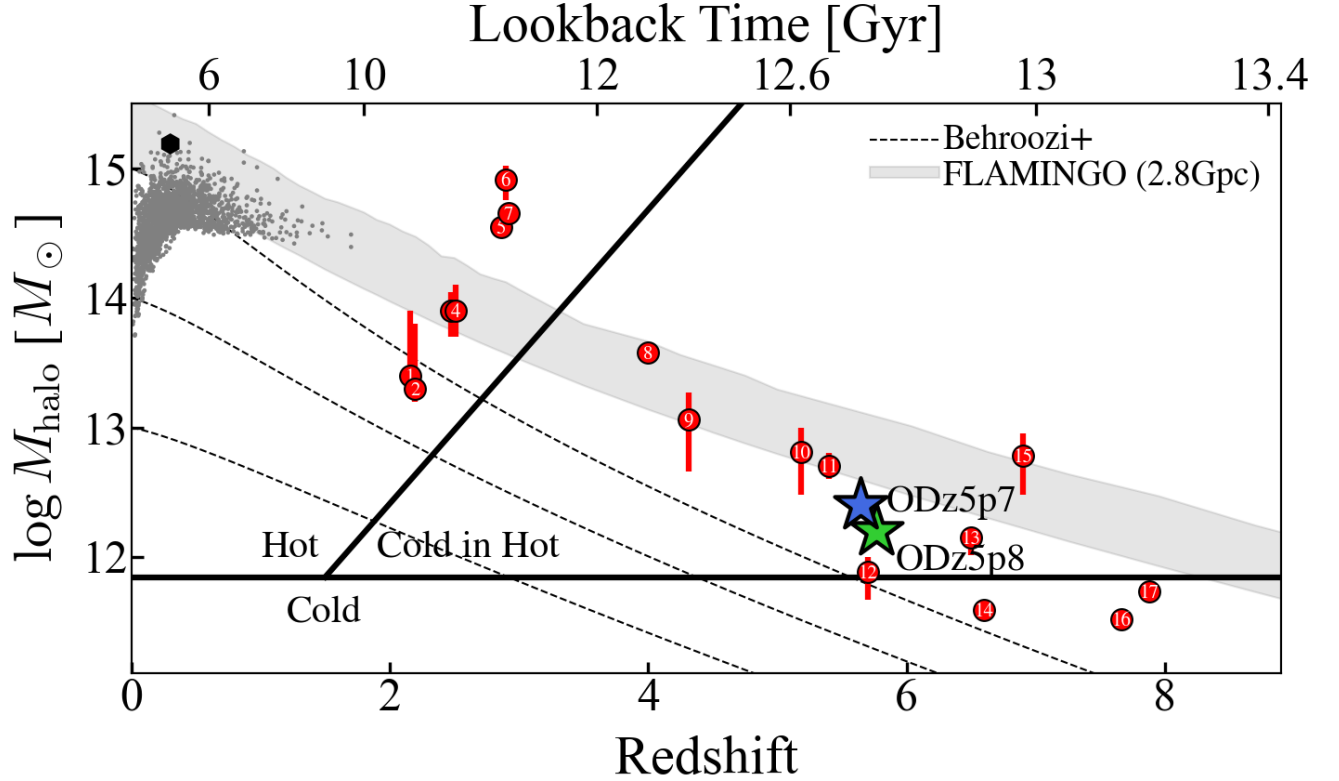


**Figure 4.** Halo masses of the two discovered overdensities (ODz5p7 and ODz5p8; star symbols), along with other (proto-) clusters and overdensities in the literature. Trajectories of massive halos ( $M_h(z=0) = 10^{13}, 10^{14}$ , and  $10^{15} M_\odot$ ) calculated using an empirical formulae (Behroozi et al. 2013, dashed lines) and of  $> 10^{15} M_\odot$  identified in the FLAMINGO simulation (Lim et al. 2024, hatched regions) are shown. Data points at  $z > 2$  are: 1 and 2 (Polletta et al. 2021; Koyama et al. 2021), 3 (Casey et al. 2015), 4 (Wang et al. 2016), 5 (Venemans et al. 2007), 6 (Cucciati et al. 2014), 7 (Venemans et al. 2007), 8 (Oteo et al. 2018), 9 (Miller et al. 2018), 10 (Sun et al. 2023), 11 (Helton et al. 2024), 12 (Harikane et al. 2019), 13 (Chanchaiworawit et al. 2019), 14 (Harikane et al. 2019), 15 (Arribas et al. 2023), 16 (Laporte et al. 2022), 17 (Morishita et al. 2023). Data points at  $z < 2$  (gray) are SPT clusters presented in Bocquet et al. (2018) and X-ray-SZ clusters in Tarrío et al. (2019). The three different gas cooling regimes (cold, hot, and cold in hot) predicted by Dekel & Birnboim (2006) are shown. In the hot regime, cold flows are expected not to reach the central galaxy due to shock heating. The halo mass of A2744OD7p9 has been updated from the one estimated in Morishita et al. (2023) to  $5.4 \pm 0.1 \times 10^{11} M_\odot$ , by including three newly confirmed sources (Hashimoto et al. 2023; Chen et al. 2024). The total mass of the cluster Abell 2744 estimated in Finner et al. (2024) is also shown (black hexagon).

track from stellar population synthesis, generated with `fsps` (Conroy et al. 2009). We find that all wELGs follow the track of a single, short burst model (i.e. SSP), whereas the majority of non-wELGs follow the track of a constant star formation model. This indicates that the origin of strong Balmer break in wELGs is likely attributed to their shorter duration of star formation, instead of wELGs being formed earlier than non-wELGs.

It is noted that dust attenuation could mildly increase the  $D_e4000$  measurement too. However, most of our sample galaxies have extinction below  $A_V < 0.5$  mag (Tab. 1), and we find no statistical difference in dust attenuation between the field sample and the overdensity members, suggesting that dust attenuation by itself does not contribute to the observed offset seen between the two samples.

There are a few non-wELGs that exhibit relatively strong 4000 Å break,  $\gtrsim 1.5$ . One of them, ID53527, shows evidence of line broadening in its emission lines, suggesting the presence of AGN. The other two show no clear evidence of AGN. We discuss potential contributions of AGN to the shutdown of star formation in Sec. 5.3. We note that these non-wELGs are all found within the discovered overdensities.

## 5. DISCUSSION

### 5.1. On the selection completeness of our sample

Our study is limited by incompleteness and pre-selection of sources for the MSA observations. While NIRCcam WFSS offers an unbiased identification of emitters, it does not cover the wavelengths of  $H\alpha + [N II]$  or 4000 Å break, which are the key measurements in our



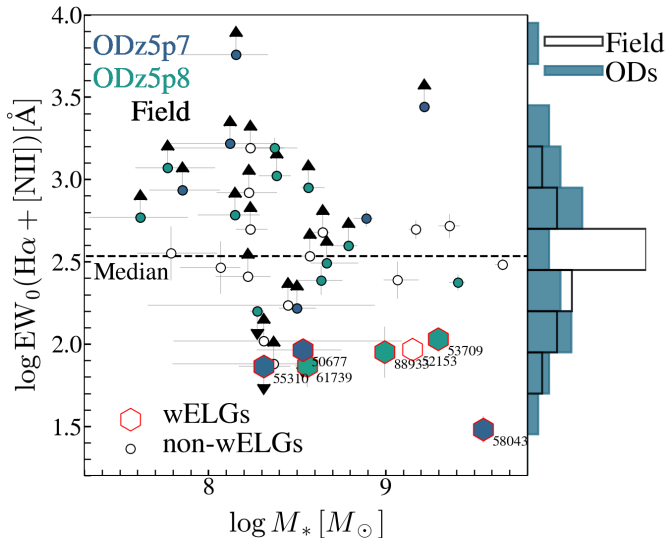


**Figure 5.** Distribution of  $H\alpha+[N II]$  rest-frame equivalent width measurements of the overdensity samples (filled symbols) and the field samples (open symbols).  $2\text{-}\sigma$  lower limits are shown for those with the continuum undetected (arrows). Those with  $EW_0(H\alpha+[N II]) \lesssim 100 \text{ \AA}$  are defined as weak emission line galaxies (wELGs; hexagons). IDs are shown only for wELGs. A high fraction (6/7) of wELGs are found in one of the overdensities. The median value measured for the entire sample is shown (horizontal dashed line).

discussion in the following sections. The WFSS samples, on the other hand, are found primarily within the two overdensities. In fact, as seen in Sec. 4.1, the fraction of wELGs in the two overdensities is still significantly higher than in the field sample, regardless of assumptions that all WFSS are wELGs or non-wELGs. As such, our conclusion remains the same regardless of the limitation.

We also note that our selection relies on the detection of strong emission lines, and is likely incomplete for quenched galaxies. The MSA sensitivity limit for  $H\alpha+[N II]$  equivalent width measurements is  $\sim 10\text{--}50 \text{ \AA}$ . However, among our photometric samples that were selected in Sec. 2.1 ( $N = 67$ ), we find no galaxies that are classified as passive e.g. on the  $UVJ$  color diagram, nor  $\log M_*/M_\odot \gtrsim 10$  galaxies. As such, in the following discussion we assume that the identified sources well represent the majority of the member galaxies in the two discovered overdensities.

### 5.2. On the High Observed Frequency of Evolved Galaxies in Overdensities

In previous sections, we have seen that a large fraction of galaxies in the two discovered overdensities exhibit a small  $EW_0(H\alpha+[N II])$ . While the  $H\alpha+[N II]$  lines cannot completely be deblended with the NIRSpect PRISM resolution, the line ratio is typically found to

be  $[N II]/H\alpha \sim 0.1$  in star-forming galaxy populations at similar redshifts (e.g., Sanders et al. 2023). In a case with AGN, the contribution from  $[N II]$  becomes larger. As such, under either of the assumptions, the measured equivalent width of  $H\alpha+[N II]$  serves as a conservative indicator of ongoing star formation.

Figure 5 shows that galaxies in the two overdensities occupy the bottom-right area, whereas we see both overdensity and field galaxies in the middle-to-high  $H\alpha+[N II]$  range. The absence of sources in the bottom-left area is likely due to the incompleteness originating in the spectroscopic sensitivity. These observations indicate that star formation in *some* galaxies in the two overdensities is systematically suppressed compared to the field samples.

We have seen in Sec. 4.2 that all selected wELGs are consistent with a SSP-like star formation history, whereas many non-wELG samples follow the trajectory of a continuous star formation history. On the other hand, the age distribution of wELGs and non-wELGs is found to be similar, except for the dominance of (both overdensity and field) non-wELGs at a very young age. From this comparison, it is suggested that wELGs are populations of galaxies that experienced a shorter duration star formation, but not necessarily formed earlier than the field samples.

These findings are overall consistent with studies of galaxies in lower redshift clusters and groups, where a large fraction of post-starburst galaxies is seen (e.g., Dressler & Gunn 1983; Dressler et al. 1999; Balogh et al. 1999; Paccagnella et al. 2017, 2019). The physical origin of starbursts and the rapid shutdown of star formation in cluster environments have intensively been discussed, attributing to ram pressure stripping (e.g., Poggianti et al. 2009; Vulcani et al. 2020; Werle et al. 2022). Their origin in early overdensities is still an open question. Being at high redshift, our study is in a position to offer a unique perspective into initial assembly and growth.

For our redshift range, overdensities are in general considered to be associated to abundance of gas (e.g., Casey 2016; Noble et al. 2017; Pensabene et al. 2024). There, galaxy star formation activity could be enhanced. The presence of *high*  $EW_0(H\alpha+[N II])$  emitters ( $\gtrsim 1000 \text{ \AA}$ ), not only of wELGs, in overdensities supports the idea. For galaxies to have a systematically reduced SFR in such gas abundance environments, *even stronger* regulation of star formation would be required.

For the observed established continuum break seen in many wELGs, regulation by negative feedback from the recent starburst seems to be a straightforward consideration. In particular, considering the relatively small masses of the wELG samples ( $\log M_*/M_\odot \sim 8.4\text{--}9.5$ ),

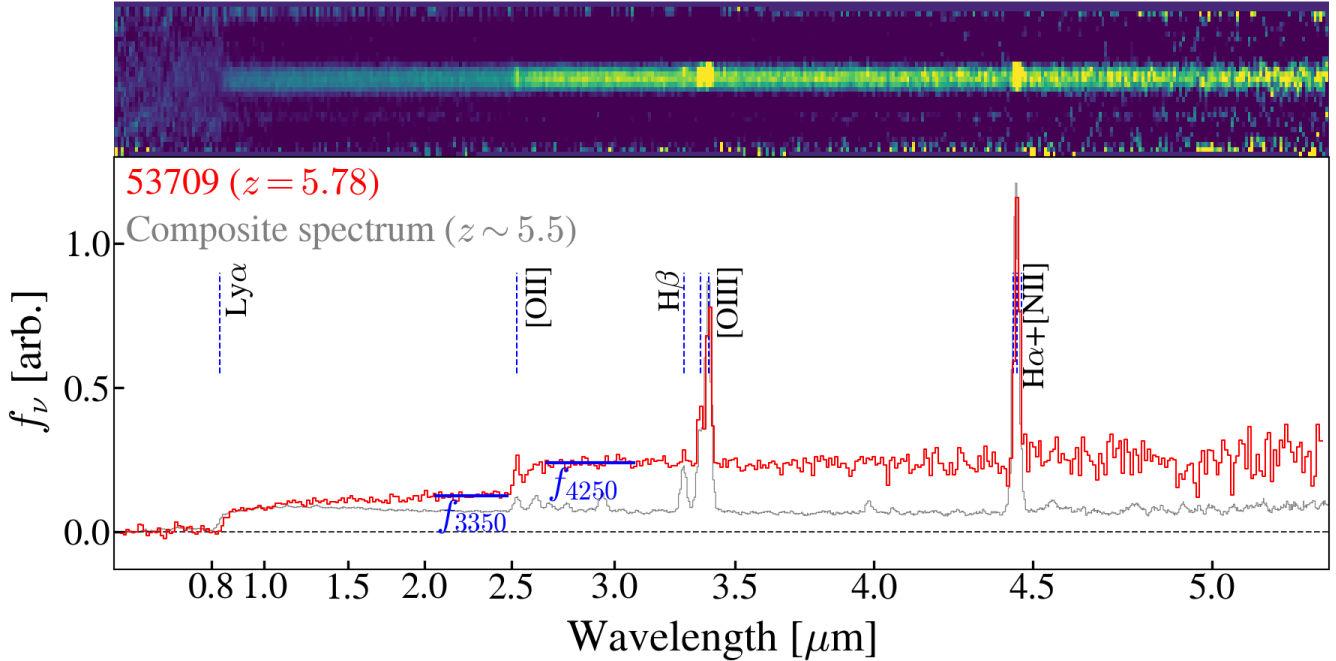


**Figure 6.** One of weak emission line galaxies (wELGs; Sec. 4.1). This example showcases a prominent continuum (4000 Å+Balmer) break, measured by the ratio  $f_{4250}/f_{3350}$ , indicating the presence of evolved ( $\approx 100$  Myr) stellar populations. Compared is the average spectrum of  $z \sim 5.5$  galaxies (gray line) from Roberts-Borsani et al. (2024).

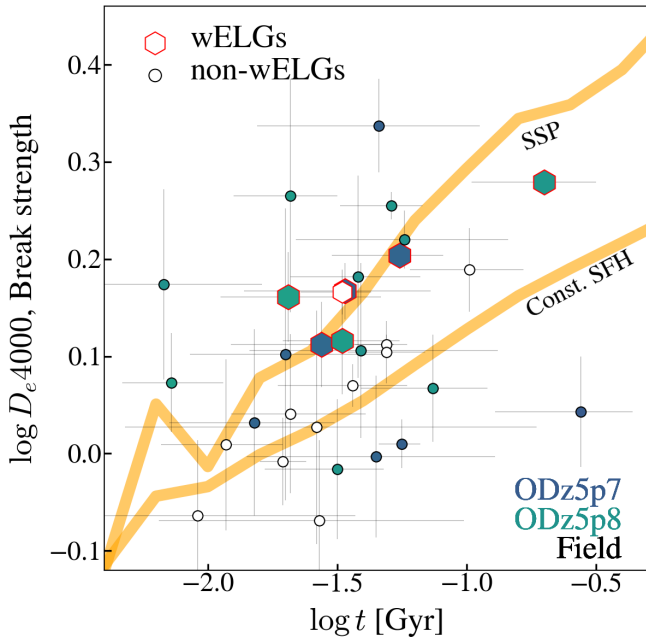


**Figure 7.** NIRSpec samples. Only those with the  $D_e4000$  break securely measured (with the uncertainty of  $< 0.1$  dex) are shown. Galaxies with a reduced  $H\alpha+[N II]$  (i.e. wELGs; hexagons) exhibit a stronger continuum break strength than non-wELGs for a given light-weighted age ( $t$ , derived in the SED analysis in Sec. 2.1). The two evolutionary tracks, single burst (SSP) and constant star formation models, are shown (red solid lines). The wELGs follow the SSP track, indicating that they experienced a short-duration star formation.

they are more vulnerable to such feedback than typical quenched galaxies ( $\log M_*/M_\odot \gg 10$ ) are. What is not obvious is if supernova feedback from a single starburst could quench subsequent star formation activity. “Mini-quenching” is one of recently proposed scenarios (Dome et al. 2024), to explain the presence of similarly low-mass galaxies with a reduced star formation rate in the early universe (Looser et al. 2023; Strait et al. 2023). A toy model indicates that a single star formation event can halt star formation, but only lasts for  $\sim 20$ – $40$  Myr (also Faisst & Morishita 2024). If overdensity environments somehow extend the duration of quenching, it would reasonably explain the observed high frequency of wELGs in the two overdensities, aside from any potential contribution from AGN, which we revisit in Sec. 5.3.

On the other hand, since their masses are relatively low, it takes less environment heating to remove/heat up gas in an individual galaxy, quenching it. However, given the available timescale by the observed redshift, environmental quenching via, e.g., ram pressure stripping due to galaxies moving within the ICM and interactions after infall (e.g., Peng et al. 2010; Wetzell et al. 2012) is not expected to be the dominant quenching channel. In fact, none of our galaxies show clear evidence of ram-pressure stripping in NIRCcam images. In a massive halo, gas heating mechanisms from virial shock can prevent infalling gas to reach to the center (e.g., Dekel & Birnboim 2006; Daddi et al. 2022). However,

the estimated halo masses of the two overdensities could be too small for this to happen either. The two overdensities are located in the predicted regime where cold gas can still penetrate through hot media and reach to the central galaxy (Fig. 4).

It is worth noting that studies of higher redshift (proto-) clusters have shown consistent pictures but somewhat at a weaker significance. Morishita et al. (2023) reported that the member galaxies of A2744ODz7p9, a protocluster at  $z = 7.88$ , have a recent, short-duration star formation of an order of  $\Delta t \lesssim 100$  Myr. Hashimoto et al. (2023) reported that the member galaxies of the same protocluster have a systematically redder UV slope  $\beta_{UV}$  than field samples. Li et al. (2024) confirmed the similar trend using a larger sample of galaxies in various environments over a wider redshift range. However, given the  $\beta_{UV}$  measurement is sensitive to the enhancement of dust, it remained unclear if the redder slope can be attributed to the reduction of star formation in those member galaxies. In fact, the majority of the  $z = 7.88$  protocluster show disturbed morphologies, indicative of recent/ongoing mergers. The direct measurements of  $H\alpha$  and continuum break strength in this study, on the other hand, have offered a more straightforward insight into the decline of star formation in overdensities. Witten et al. (2024) recently reported a strong Balmer break and weak emission lines in one of the protocluster member galaxies, similar to the population of wELGs reported in our study.

### 5.3. The Potential Contributions by AGN on the Reduced Star Formation Activities

The presence of AGN is critical in understanding the mechanism responsible for reduction in star formation inferred from  $EW_0(H\alpha + [N II])$ . With the spectral resolution of the PRISM spectra, however, our ability of identifying AGN candidates is limited. To further investigate the presence of AGN, we show our samples on the Mass-Excitation (MEx) diagram in Fig. 8, which offers an empirical classification for AGN (Juneau et al. 2014).

Firstly, among all wELGs, there is one that shows a significantly high line ratio (ID53709,  $[O III]/H\beta > 25$  at  $2\sigma$ ), making itself a very likely candidate of AGN. In addition, the observed  $H\alpha + [N II]/H\beta$  ratio of the same source,  $\gtrsim 38$  at  $2\sigma$ , is extremely high, potentially driven by a strong  $[N II]$  emission. However, despite the high significance of emission line detection (Fig. 6), the spectrum does not show evidence of line broadening. The continuum spectrum of this source is characterized well by the underlying evolved stellar populations. These characteristics are seen in typical Seyfert 2 galaxies. For

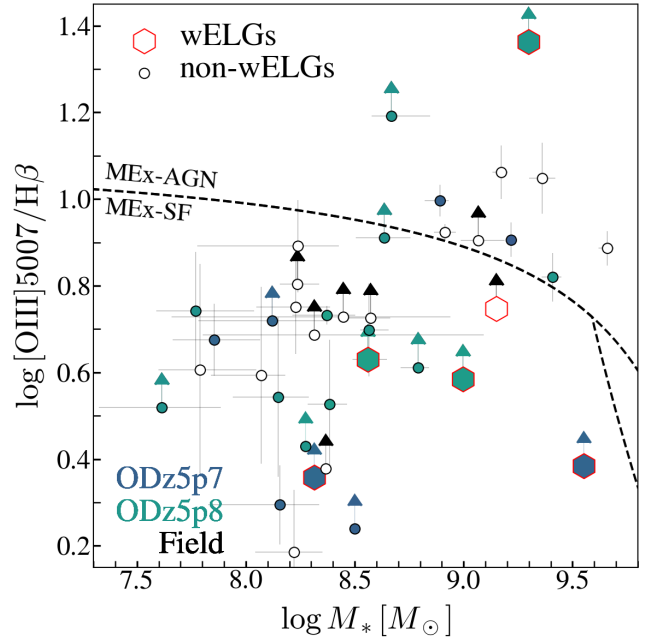


**Figure 8.** Our samples in the stellar mass-excitation (MEx) diagram. For those with  $H\beta$  undetected, a  $2\sigma$  lower limit is shown. Colors and symbols are as shown in Fig. 5. We do not see the dominance of potential AGN in the overdensity samples.

the observed  $[O III]/H\beta$  ratio,  $[N II]/H\alpha$  is expected to be  $\sim 1-3$ , by taking the measurements for the Sloan Seyfert 2 galaxies (e.g., Kauffmann et al. 2003; Malkan et al. 2017). This indicates that the actual star formation activity in the source is even smaller.

Secondly, we revisit those with strong Balmer break but with a higher  $EW_0(H\alpha + [N II])$  than  $100 \text{ \AA}$  (IDs 53527, 59993, 48996), including the one showing a broad line (ID53527). These sources are an important population for our understanding of the potential origin of wELGs. All the three objects above are classified as MEx-AGN. In fact, while they are not selected as wELGs, all three sources have relatively weak  $H\alpha$  emissions, with  $EW_0(H\alpha + [N II])$  ranging  $\sim 200-300 \text{ \AA}$ . Also noted is that AGN typically have a higher  $[N II]/H\alpha$  ratio. As such, their actual star formation activity may be even more reduced than what is inferred from  $EW_0(H\alpha + [N II])$ . Therefore, we speculate that these non-wELGs are likely the intermediate populations, under the influence of AGN on their star formation activity, and may end up to more quiescent populations like wELGs.

We note that the connection between wELGs and non-wELGs appears to be what is seen in the local universe, especially for those with high  $[O III]$ -to- $H\beta$  ratio. In the Sloan sample, the right wing in the BPT diagram (i.e.

high  $[\text{O III}]/\text{H}\beta$  and  $[\text{N II}]/\text{H}\alpha$ ) is populated by both bona-fide AGN and ‘retired’ galaxies (e.g., Cid Fernandes et al. 2010). The mass range of the wELG samples is considered relatively smaller than the typical mass at which the impact from AGN on the host galaxy becomes crucial (Di Matteo et al. 2005; Hopkins et al. 2006; Somerville et al. 2008). Despite, numerical studies (e.g., Koudmani et al. 2021) found that even at this low mass range AGN can be influential, due to the small potential well of the system and potential overmassive BHs at this cosmic time (Izumi et al. 2021; Kocevski et al. 2023; Übler et al. 2023). Given the prevalence of AGN in low-mass galaxies found by recent JWST observations (Harikane et al. 2023; Matthee et al. 2023; Maiolino et al. 2023), AGN could be an equally possible quenching scenario.

A missing link is, then, if the occurrence of AGN is related to the nature of overdensities, which is under much debate (e.g., Overzier 2016; Macuga et al. 2019; Gatica et al. 2024). Theoretical studies predict a higher AGN fraction in overdensities compared to average fields, due to increased gas fractions and higher merger rates. However, it remains unknown whether such distinctions appear as early as  $t_{\text{cosmo}} < 1$  Gyr, especially considering the presence of negative feedback (e.g., Stiavelli 2005; Kim et al. 2009). Indeed, we observed one potential AGN (ID43506, i.e. Little Red Dot) in isolation. A robust determination of the AGN fraction in early overdensities with a larger sample would provide an invaluable benchmark and help us understand their interplay with overdensities.

## 6. SUMMARY AND FUTURE PROSPECT

In this study, we identified two overdensities of galaxies at  $z \sim 5.7$  in the sightline of the galaxy cluster Abell 2744. Combined with the sensitive JWST spectroscopic data, these unique early overdensities allowed us to conduct an in-depth investigation of both the overdensities themselves and the individual member galaxies. Remarkably, we identified six galaxies within the overdensities that show weak  $\text{H}\alpha + [\text{N II}]$  emissions ( $27 \pm 6\%$ ). The fraction of such galaxies was

found significantly lower ( $6 \pm 2\%$ ) in field samples of the equivalent redshift range. The large scatter observed in  $\text{EW}_0(\text{H}\alpha + [\text{N II}])$  of the overdensity samples suggests that overdensities are places where star formation can be enhanced too. Taken together, these observations suggest that environments may be influential to galaxy evolution as early as within the first billion years after the Big Bang, leading to the accelerated maturation of galaxies as seen in lower redshift clusters and groups. While the exact physical mechanisms at play are yet to be investigated, our observations support the idea that feedback from intense star formation self-regulates subsequent star formation in overdensities, leading to an increased fraction of wELGs compared to the average field. While AGN may contribute to the observed quiescence, their dominance in overdense environments remains unclear.

The evolutionary link of the wELGs identified here to massive, quenched galaxy populations at lower redshifts, discovered by recent JWST spectroscopic studies (Carnall et al. 2023; de Graaff et al. 2024), is another point of interest. Predicting the future evolution of individual systems is challenging. However, we note that the stellar mass of wELGs in our samples is small, and they are unlikely to be the direct progenitor of quenched populations of  $\sim 10^{11} M_{\odot}$  by  $z \sim 4$ . In addition, given the low star formation rate of wELGs, the mass gap between the two populations seems challenging to fill solely with intrinsic star formation, unless there is an abundance of gas reservoirs available. An alternative scenario is that most of the member galaxies will merge into a single system, which would ease the tension. However, the timescale for this to happen is not obvious and needs verification through numerical calculations. Future searches for wELGs to a larger extent will give us an improved view of the origin of these systems. If we still fail to find more massive wELGs in a larger sample, it would suggest that the majority of massive quenched galaxy populations were either formed in isolated environments or through a number of mergers in early density peaks. Direct confirmation of this can also be achieved by investigating the surrounding environment of massive quenched galaxies at lower redshifts.

**Table 1.**

| ID | R.A. | Decl. | $z$ | inst | $\mu$ | $\log M_{\star}$ | $\log \text{SFR}$          | $\log t$ | $\text{EW}_0(\text{H}\alpha + [\text{N II}])$ | $\log D_e 4000$ | $\log[\text{O III}]/\text{H}\beta$ |
|----|------|-------|-----|------|-------|------------------|----------------------------|----------|---|-----------------|------------------------------------|
|    | deg. | deg.  |     |      |       | $M_{\odot}$      | $M_{\odot} \text{yr}^{-1}$ | Gyr      | $\text{\AA}$                                  |                 |                                    |

**Table 1** *continued*

Table 1 (continued)

| ID                             | R.A.    | Decl.     | $z$    | inst | $\mu$                | $\log M_*$          | $\log \text{SFR}$        | $\log t$             | $\text{EW}_0(\text{H}\alpha + [\text{N II}])$ | $\log D_e4000$   | $\log[\text{O III}]/\text{H}\beta$ |
|--------------------------------|---------|-----------|--------|------|----------------------|---------------------|--------------------------|----------------------|---|------------------|------------------------------------|
|                                | deg.    | deg.      |        |      |                      | $M_\odot$           | $M_\odot \text{yr}^{-1}$ | Gyr                  | $\text{\AA}$                                  |                  |                                    |
| ODz5p7 ( $5.640 < z < 5.680$ ) |         |           |        |      |                      |                     |                          |                      |   |                  |                                    |
| 80595                          | 3.51062 | -30.30537 | 5.6450 | msa  | $1.2^{+0.1}_{-0.1}$  | $9.2^{+0.1}_{-0.1}$ | $0.3^{+0.1}_{-0.1}$      | $-0.6^{+0.2}_{-0.3}$ | > 2760  | $0.04 \pm 0.06$  | $0.9 \pm 0.1$                      |
| 50956                          | 3.60621 | -30.38662 | 5.6550 | wfss | $2.0^{+0.1}_{-0.1}$  | $9.4^{+0.1}_{-0.1}$ | $0.9^{+0.1}_{-0.1}$      | $-0.9^{+0.1}_{-0.1}$ | –   | –                | –                                  |
| 49662                          | 3.62365 | -30.38427 | 5.6556 | wfss | $1.5^{+0.1}_{-0.1}$  | $9.2^{+0.1}_{-0.1}$ | $0.7^{+0.1}_{-0.2}$      | $-1.0^{+0.1}_{-0.1}$ | –   | –                | –                                  |
| 53131                          | 3.59074 | -30.37940 | 5.6565 | wfss | $2.8^{+0.1}_{-0.1}$  | $8.6^{+0.1}_{-0.1}$ | $0.8^{+0.1}_{-0.1}$      | $-1.5^{+0.1}_{-0.2}$ | –   | –                | –                                  |
| 55048                          | 3.60194 | -30.35852 | 5.6570 | msa  | $1.9^{+0.1}_{-0.1}$  | $8.5^{+0.1}_{-0.1}$ | $0.4^{+0.9}_{-0.8}$      | $-1.3^{+0.4}_{-0.5}$ | > 165   | $0.34 \pm 0.05$  | –                                  |
| 53596                          | 3.58709 | -30.37909 | 5.6570 | wfss | $3.2^{+0.1}_{-0.1}$  | $7.8^{+0.2}_{-0.3}$ | $0.3^{+0.2}_{-0.2}$      | $-1.7^{+0.3}_{-0.3}$ | –   | –                | –                                  |
| 49572                          | 3.62461 | -30.38420 | 5.6573 | wfss | $1.5^{+0.1}_{-0.1}$  | $9.0^{+0.1}_{-0.1}$ | $0.7^{+0.3}_{-0.2}$      | $-1.3^{+0.2}_{-0.2}$ | –   | –                | –                                  |
| 56326                          | 3.55999 | -30.38286 | 5.6590 | wfss | $3.9^{+0.3}_{-0.3}$  | $8.6^{+0.1}_{-0.1}$ | $0.7^{+0.2}_{-0.1}$      | $-1.1^{+0.1}_{-0.1}$ | –   | –                | –                                  |
| 50677                          | 3.62013 | -30.37873 | 5.6590 | msa  | $1.6^{+0.1}_{-0.1}$  | $8.5^{+0.2}_{-0.3}$ | $0.6^{+0.7}_{-0.8}$      | $-1.5^{+0.3}_{-0.4}$ | < 92 <sup>†</sup>                             | $0.17 \pm 0.03$  | –                                  |
| 51298                          | 3.59069 | -30.39555 | 5.6600 | msa  | $10.0^{+0.8}_{-0.6}$ | $8.9^{+0.1}_{-0.1}$ | $1.5^{+0.1}_{-0.1}$      | $-1.2^{+0.1}_{-0.1}$ | $578 \pm 70$                                  | $0.01 \pm 0.03$  | $1.0 \pm 0.1$                      |
| 51543                          | 3.57611 | -30.40446 | 5.6600 | wfss | $2.9^{+0.1}_{-0.1}$  | $8.6^{+0.1}_{-0.2}$ | $0.8^{+0.1}_{-0.1}$      | $-1.5^{+0.1}_{-0.1}$ | –   | –                | –                                  |
| 58759                          | 3.58166 | -30.35060 | 5.6650 | msa  | $4.4^{+0.9}_{-0.6}$  | $7.9^{+0.2}_{-0.2}$ | $0.6^{+0.4}_{-0.4}$      | $-1.8^{+0.3}_{-0.3}$ | > 862   | $0.03 \pm 0.10$  | $0.7 \pm 0.1$                      |
| 54365                          | 3.60026 | -30.36428 | 5.6670 | msa  | $2.0^{+0.1}_{-0.1}$  | $8.2^{+0.2}_{-0.3}$ | $0.1^{+0.3}_{-0.3}$      | $-1.4^{+0.5}_{-0.5}$ | > 5731  | $-0.00 \pm 0.08$ | $0.3 \pm 0.1$                      |
| 56103                          | 3.59928 | -30.35404 | 5.6670 | msa  | $2.1^{+0.1}_{-0.1}$  | $8.1^{+0.2}_{-0.3}$ | $0.4^{+0.3}_{-0.3}$      | $-1.7^{+0.4}_{-0.4}$ | > 1650  | $0.10 \pm 0.15$  | > 0.7                              |
| 55321                          | 3.59436 | -30.36236 | 5.6672 | wfss | $2.4^{+0.2}_{-0.1}$  | $8.5^{+0.1}_{-0.1}$ | $0.5^{+0.8}_{-0.7}$      | $-1.3^{+0.2}_{-0.3}$ | –   | –                | –                                  |
| 58043                          | 3.59316 | -30.34647 | 5.6680 | msa  | $2.0^{+0.1}_{-0.1}$  | $9.6^{+0.1}_{-0.1}$ | $1.3^{+0.1}_{-0.1}$      | $-1.3^{+0.2}_{-0.3}$ | $30 \pm 6^\dagger$                            | $0.20 \pm 0.01$  | –                                  |
| 55310                          | 3.59431 | -30.36251 | 5.6760 | msa  | $2.4^{+0.2}_{-0.1}$  | $8.3^{+0.1}_{-0.1}$ | $0.5^{+0.5}_{-0.4}$      | $-1.6^{+0.3}_{-0.3}$ | < 73 <sup>†</sup>                             | $0.11 \pm 0.04$  | –                                  |
| ODz5p8 ( $5.764 < z < 5.804$ ) |         |           |        |      |                      |                     |                          |                      |   |                  |                                    |
| 50110                          | 3.57303 | -30.41955 | 5.7642 | wfss | $1.8^{+0.1}_{-0.1}$  | $7.9^{+0.1}_{-0.1}$ | $0.2^{+0.2}_{-0.2}$      | $-1.8^{+0.4}_{-0.3}$ | –   | –                | –                                  |
| 50863                          | 3.57063 | -30.41463 | 5.7650 | msa  | $1.8^{+0.1}_{-0.1}$  | $9.4^{+0.1}_{-0.1}$ | $1.2^{+0.1}_{-0.1}$      | $-1.4^{+0.2}_{-0.3}$ | –   | –                | –                                  |
| 53429                          | 3.56483 | -30.39717 | 5.7694 | wfss | $2.2^{+0.1}_{-0.1}$  | $8.0^{+0.2}_{-0.1}$ | $0.4^{+0.2}_{-0.2}$      | $-1.6^{+0.2}_{-0.2}$ | –   | –                | –                                  |
| 49882                          | 3.60542 | -30.39658 | 5.7710 | msa  | $2.2^{+0.1}_{-0.1}$  | $7.8^{+0.3}_{-0.2}$ | $0.1^{+0.2}_{-0.1}$      | $-1.7^{+0.2}_{-0.2}$ | > 1176  | –                | $0.7 \pm 0.1$                      |
| 89694                          | 3.47607 | -30.31035 | 5.7710 | msa  | $1.2^{+0.1}_{-0.1}$  | $8.1^{+0.1}_{-0.2}$ | $-0.2^{+0.7}_{-0.7}$     | $-1.4^{+0.5}_{-0.4}$ | > 606   | $0.11 \pm 0.09$  | $0.5 \pm 0.2$                      |
| 46821                          | 3.58522 | -30.43137 | 5.7710 | msa  | $1.7^{+0.1}_{-0.1}$  | $7.6^{+0.3}_{-0.3}$ | $0.2^{+0.4}_{-0.4}$      | $-2.2^{+0.4}_{-0.2}$ | > 586   | $0.17 \pm 0.10$  | > 0.5                              |
| 53423                          | 3.56492 | -30.39715 | 5.7717 | wfss | $2.2^{+0.1}_{-0.1}$  | $8.6^{+0.1}_{-0.1}$ | $0.8^{+0.1}_{-0.1}$      | $-1.6^{+0.2}_{-0.2}$ | –   | –                | –                                  |
| 48996                          | 3.61314 | -30.39705 | 5.7720 | msa  | $2.0^{+0.1}_{-0.1}$  | $8.7^{+0.2}_{-0.1}$ | $0.6^{+0.1}_{-0.1}$      | $-1.4^{+0.2}_{-0.3}$ | > 310   | $0.18 \pm 0.10$  | > 1.2                              |
| 53846                          | 3.56520 | -30.39427 | 5.7730 | msa  | $2.4^{+0.1}_{-0.1}$  | $8.8^{+0.1}_{-0.1}$ | $1.4^{+0.1}_{-0.2}$      | $-1.9^{+0.2}_{-0.3}$ | –   | –                | –                                  |
| 59993                          | 3.55409 | -30.36362 | 5.7740 | msa  | $2.7^{+0.2}_{-0.2}$  | $8.6^{+0.1}_{-0.1}$ | $0.5^{+0.5}_{-0.4}$      | $-1.2^{+0.4}_{-0.4}$ | $243 \pm 54$                                  | $0.22 \pm 0.03$  | > 0.9                              |
| 93770                          | 3.45971 | -30.31249 | 5.7750 | msa  | $1.2^{+0.1}_{-0.1}$  | $8.3^{+0.1}_{-0.1}$ | $-0.2^{+0.2}_{-0.1}$     | $-1.1^{+0.2}_{-0.3}$ | < 157   | $0.07 \pm 0.06$  | –                                  |
| 48689                          | 3.61923 | -30.39446 | 5.7750 | wfss | $1.7^{+0.1}_{-0.1}$  | $9.6^{+0.1}_{-0.1}$ | $1.3^{+0.2}_{-0.1}$      | $-1.3^{+0.2}_{-0.3}$ | –   | –                | –                                  |
| 50756                          | 3.61025 | -30.38559 | 5.7756 | wfss | $1.8^{+0.1}_{-0.1}$  | $9.0^{+0.1}_{-0.1}$ | $1.0^{+0.1}_{-0.1}$      | $-1.6^{+0.2}_{-0.2}$ | –   | –                | –                                  |
| 84406                          | 3.48715 | -30.31302 | 5.7790 | msa  | $1.2^{+0.1}_{-0.1}$  | $8.8^{+0.1}_{-0.1}$ | $-0.1^{+0.3}_{-0.3}$     | $-0.8^{+0.2}_{-0.3}$ | > 396   | –                | > 0.6                              |
| 53527                          | 3.56109 | -30.39926 | 5.7790 | msa  | $1.9^{+0.1}_{-0.1}$  | $9.4^{+0.1}_{-0.1}$ | $1.3^{+0.1}_{-0.1}$      | $-1.3^{+0.1}_{-0.2}$ | $236 \pm 27$                                  | $0.26 \pm 0.01$  | $0.8 \pm 0.1$                      |
| 53486                          | 3.56110 | -30.39932 | 5.7799 | wfss | $1.9^{+0.1}_{-0.1}$  | $9.1^{+0.1}_{-0.1}$ | $1.2^{+0.1}_{-0.1}$      | $-1.5^{+0.1}_{-0.2}$ | –   | –                | –                                  |
| 94381                          | 3.46566 | -30.30868 | 5.7830 | msa  | $1.2^{+0.1}_{-0.1}$  | $8.6^{+0.1}_{-0.1}$ | $0.3^{+0.1}_{-0.1}$      | $-1.5^{+0.2}_{-0.3}$ | > 891   | $-0.02 \pm 0.07$ | $0.7 \pm 0.1$                      |
| 53709                          | 3.59614 | -30.37138 | 5.7840 | msa  | $2.3^{+0.1}_{-0.1}$  | $9.3^{+0.1}_{-0.1}$ | $0.6^{+0.1}_{-0.1}$      | $-0.7^{+0.2}_{-0.3}$ | $107 \pm 7^\dagger$                           | $0.28 \pm 0.01$  | > 1.4                              |

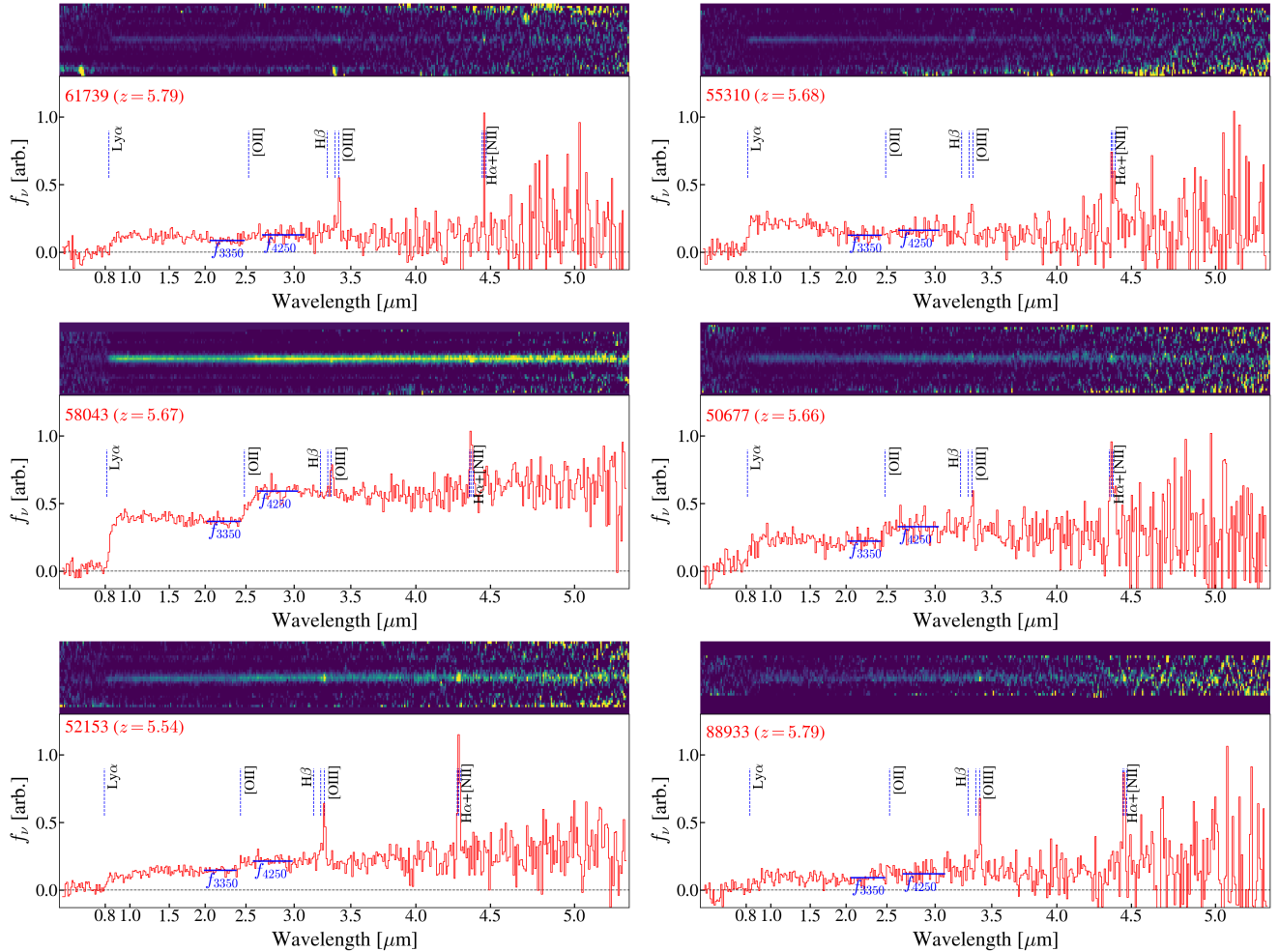
Table 1 continued



Table 1 (continued)

| ID           | R.A.    | Decl.     | $z$    | inst | $\mu$                | $\log M_*$          | $\log \text{SFR}$        | $\log t$             | $\text{EW}_0(\text{H}\alpha + [\text{N II}])$ | $\log D_e4000$   | $\log[\text{O III}]/\text{H}\beta$ |
|--------------|---------|-----------|--------|------|----------------------|---------------------|--------------------------|----------------------|---|------------------|------------------------------------|
|              | deg.    | deg.      |        |      |                      | $M_\odot$           | $M_\odot \text{yr}^{-1}$ | Gyr                  | $\text{\AA}$                                  |                  |                                    |
| 93880        | 3.46578 | -30.30868 | 5.7850 | msa  | $1.2^{+0.1}_{-0.1}$  | $8.4^{+0.1}_{-0.1}$ | $0.3^{+0.1}_{-0.1}$      | $-1.7^{+0.2}_{-0.2}$ | $> 1051$                                      | $0.27 \pm 0.12$  | $0.5 \pm 0.1$                      |
| 88933        | 3.46682 | -30.31909 | 5.7900 | msa  | $1.2^{+0.1}_{-0.1}$  | $9.0^{+0.1}_{-0.1}$ | $0.7^{+0.1}_{-0.1}$      | $-1.5^{+0.2}_{-0.2}$ | $89 \pm 38^\dagger$                           | $0.12 \pm 0.06$  | $> 0.6$                            |
| 51797        | 3.56117 | -30.41380 | 5.7920 | wfss | $1.6^{+0.1}_{-0.1}$  | $8.3^{+0.3}_{-0.3}$ | $0.3^{+0.9}_{-0.8}$      | $-1.6^{+0.3}_{-0.3}$ | –   | –                | –                                  |
| 61739        | 3.57488 | -30.33753 | 5.7950 | msa  | $1.9^{+0.1}_{-0.1}$  | $8.6^{+0.1}_{-0.1}$ | $0.7^{+0.5}_{-0.5}$      | $-1.7^{+0.4}_{-0.3}$ | $73 \pm 25^\dagger$                           | $0.16 \pm 0.05$  | $> 0.6$                            |
| 58700        | 3.54281 | -30.38065 | 5.7950 | msa  | $2.7^{+0.3}_{-0.2}$  | $8.4^{+0.1}_{-0.2}$ | $1.2^{+0.1}_{-0.1}$      | $-2.1^{+0.2}_{-0.2}$ | $1553 \pm 230$                                | $0.07 \pm 0.05$  | $0.7 \pm 0.1$                      |
| 53055        | 3.55982 | -30.40371 | 5.7958 | wfss | $1.8^{+0.1}_{-0.1}$  | $8.0^{+0.2}_{-0.3}$ | $-0.2^{+0.5}_{-0.5}$     | $-1.4^{+0.5}_{-0.5}$ | –   | –                | –                                  |
| 51150        | 3.59144 | -30.39667 | 5.8034 | wfss | $10.6^{+0.8}_{-0.6}$ | $7.7^{+0.1}_{-0.1}$ | $0.4^{+0.2}_{-0.1}$      | $-1.5^{+0.2}_{-0.3}$ | –   | –                | –                                  |
| Field Sample |         |           |        |      |                      |                     |                          |                      |   |                  |                                    |
| 68601        | 3.51938 | -30.35446 | 5.5250 | msa  | $1.8^{+0.1}_{-0.1}$  | $8.1^{+0.1}_{-0.2}$ | $0.1^{+0.4}_{-0.3}$      | $-1.5^{+0.3}_{-0.3}$ | $290 \pm 129$                                 | $-0.25 \pm 0.09$ | $0.6 \pm 0.2$                      |
| 71184        | 3.50563 | -30.34941 | 5.5250 | msa  | $1.5^{+0.1}_{-0.1}$  | $8.2^{+0.2}_{-0.2}$ | $0.3^{+0.4}_{-0.4}$      | $-1.7^{+0.3}_{-0.2}$ | $> 833$                                       | $0.04 \pm 0.08$  | $0.8 \pm 0.1$                      |
| 52836        | 3.61310 | -30.36461 | 5.5269 | wfss | $1.6^{+0.1}_{-0.1}$  | $9.0^{+0.1}_{-0.1}$ | $1.0^{+0.1}_{-0.1}$      | $-1.5^{+0.1}_{-0.1}$ | –   | –                | –                                  |
| 55293        | 3.60640 | -30.35339 | 5.5350 | msa  | $1.7^{+0.1}_{-0.1}$  | $8.4^{+0.2}_{-0.6}$ | $0.3^{+1.3}_{-1.3}$      | $-1.6^{+0.5}_{-0.5}$ | $> 75$  | –                | –                                  |
| 49775        | 3.58499 | -30.41307 | 5.5360 | wfss | $3.5^{+0.1}_{-0.1}$  | $8.2^{+0.1}_{-0.1}$ | $0.3^{+0.1}_{-0.1}$      | $-1.1^{+0.1}_{-0.1}$ | –   | –                | –                                  |
| 52153        | 3.57006 | -30.40369 | 5.5450 | msa  | $2.1^{+0.1}_{-0.1}$  | $9.2^{+0.1}_{-0.1}$ | $1.2^{+0.1}_{-0.1}$      | $-1.5^{+0.1}_{-0.2}$ | $92 \pm 16^\dagger$                           | $0.17 \pm 0.02$  | $> 0.7$                            |
| 51129        | 3.56063 | -30.42030 | 5.5513 | wfss | $1.5^{+0.1}_{-0.1}$  | $9.2^{+0.1}_{-0.1}$ | $0.6^{+0.1}_{-0.1}$      | $-0.8^{+0.1}_{-0.2}$ | –   | –                | –                                  |
| 51377        | 3.56250 | -30.41654 | 5.5516 | wfss | $1.6^{+0.1}_{-0.1}$  | $8.4^{+0.1}_{-0.1}$ | $0.0^{+0.3}_{-0.2}$      | $-1.1^{+0.2}_{-0.2}$ | –   | –                | –                                  |
| 79252        | 3.50683 | -30.31160 | 5.5880 | msa  | $1.3^{+0.1}_{-0.1}$  | $8.2^{+0.1}_{-0.2}$ | $0.5^{+0.4}_{-0.6}$      | $-2.1^{+0.4}_{-0.4}$ | $> 257$                                       | –                | $0.2 \pm 0.1$                      |
| 88370        | 3.46098 | -30.32513 | 5.5930 | msa  | $1.2^{+0.1}_{-0.1}$  | $8.9^{+0.1}_{-0.1}$ | $1.0^{+0.1}_{-0.1}$      | $-1.7^{+0.1}_{-0.1}$ | –   | $-0.01 \pm 0.04$ | $0.9 \pm 0.1$                      |
| 70459        | 3.51550 | -30.34624 | 5.5990 | msa  | $1.5^{+0.1}_{-0.1}$  | $9.4^{+0.1}_{-0.1}$ | $1.1^{+0.2}_{-0.2}$      | $-1.3^{+0.1}_{-0.1}$ | $520 \pm 97$                                  | $0.10 \pm 0.03$  | $1.0 \pm 0.1$                      |
| 48753        | 3.63058 | -30.38553 | 5.6080 | msa  | $1.5^{+0.1}_{-0.1}$  | $8.3^{+0.8}_{-0.5}$ | $0.3^{+3.2}_{-3.4}$      | $-1.6^{+1.1}_{-0.8}$ | $> 104$                                       | –                | $> 0.7$                            |
| 57147        | 3.57595 | -30.36545 | 5.6123 | wfss | $5.0^{+0.6}_{-0.5}$  | $8.6^{+0.1}_{-0.1}$ | $0.6^{+0.1}_{-0.1}$      | $-0.9^{+0.1}_{-0.2}$ | –   | –                | –                                  |
| 60258        | 3.55926 | -30.35749 | 5.6204 | wfss | $2.5^{+0.2}_{-0.2}$  | $9.3^{+0.1}_{-0.1}$ | $1.4^{+0.2}_{-0.2}$      | $-1.5^{+0.2}_{-0.2}$ | –   | –                | –                                  |
| 60089        | 3.56818 | -30.35228 | 5.6230 | msa  | $3.2^{+0.6}_{-0.3}$  | $7.8^{+0.3}_{-0.2}$ | $0.6^{+0.8}_{-0.9}$      | $-2.0^{+0.6}_{-0.6}$ | $355 \pm 162$                                 | $-0.06 \pm 0.08$ | $0.6 \pm 0.2$                      |
| 57351        | 3.57583 | -30.36532 | 5.6243 | wfss | $5.3^{+0.7}_{-0.6}$  | $8.2^{+0.1}_{-0.1}$ | $0.7^{+0.1}_{-0.1}$      | $-1.5^{+0.1}_{-0.1}$ | –   | –                | –                                  |
| 51117        | 3.62066 | -30.37426 | 5.6270 | msa  | $1.6^{+0.1}_{-0.1}$  | $9.7^{+0.1}_{-0.1}$ | $1.4^{+0.1}_{-0.1}$      | $-1.3^{+0.1}_{-0.1}$ | $303 \pm 26$                                  | $0.11 \pm 0.01$  | $0.9 \pm 0.1$                      |
| 60298        | 3.58610 | -30.33732 | 5.6320 | msa  | $1.8^{+0.1}_{-0.1}$  | $8.4^{+0.5}_{-0.8}$ | $0.2^{+2.0}_{-1.8}$      | $-1.6^{+0.8}_{-0.7}$ | $> 171$                                       | $0.03 \pm 0.12$  | $> 0.7$                            |
| 50110        | 3.57303 | -30.41955 | 5.7642 | wfss | $1.8^{+0.1}_{-0.1}$  | $7.9^{+0.1}_{-0.1}$ | $0.2^{+0.2}_{-0.2}$      | $-1.8^{+0.4}_{-0.3}$ | –   | –                | –                                  |
| 43506        | 3.61920 | -30.42326 | 5.8370 | msa  | $1.6^{+0.1}_{-0.1}$  | $6.9^{+0.1}_{-0.3}$ | $0.1^{+0.1}_{-0.2}$      | $-2.5^{+0.2}_{-0.3}$ | $432 \pm 24$                                  | $0.35 \pm 0.05$  | $0.4 \pm 0.1$                      |
| 53139        | 3.61317 | -30.36218 | 5.8420 | msa  | $1.6^{+0.1}_{-0.1}$  | $8.2^{+0.2}_{-0.5}$ | $-0.1^{+0.7}_{-0.6}$     | $-1.6^{+0.6}_{-0.6}$ | $> 1548$                                      | $-0.07 \pm 0.08$ | $0.9 \pm 0.1$                      |
| 69718        | 3.51380 | -30.35333 | 5.9250 | msa  | $1.7^{+0.1}_{-0.1}$  | $8.2^{+0.1}_{-0.1}$ | $0.5^{+0.2}_{-0.2}$      | $-1.9^{+0.2}_{-0.2}$ | $> 496$                                       | $0.01 \pm 0.09$  | $> 0.8$                            |
| 67911        | 3.55368 | -30.33006 | 5.9290 | msa  | $1.5^{+0.1}_{-0.1}$  | $9.1^{+0.1}_{-0.1}$ | $0.6^{+0.3}_{-0.2}$      | $-1.0^{+0.2}_{-0.2}$ | $244 \pm 73$                                  | $0.19 \pm 0.04$  | $> 0.9$                            |
| 69619        | 3.51813 | -30.35045 | 5.9320 | msa  | $1.7^{+0.1}_{-0.1}$  | $9.2^{+0.1}_{-0.1}$ | $1.0^{+0.1}_{-0.2}$      | $-1.4^{+0.2}_{-0.3}$ | $495 \pm 66$                                  | $0.07 \pm 0.02$  | $1.1 \pm 0.1$                      |
| 60260        | 3.55733 | -30.35957 | 5.9340 | wfss | $2.5^{+0.2}_{-0.1}$  | $8.3^{+0.1}_{-0.1}$ | $0.3^{+0.4}_{-0.3}$      | $-1.5^{+0.3}_{-0.3}$ | –   | –                | –                                  |
| 55866        | 3.57494 | -30.37400 | 5.9347 | wfss | $3.4^{+0.2}_{-0.2}$  | $8.6^{+0.1}_{-0.1}$ | $0.5^{+0.2}_{-0.3}$      | $-1.3^{+0.2}_{-0.3}$ | –   | –                | –                                  |
| 72143        | 3.49244 | -30.35283 | 5.9650 | msa  | $1.4^{+0.1}_{-0.1}$  | $8.6^{+0.1}_{-0.1}$ | $0.3^{+0.2}_{-0.2}$      | $-1.2^{+0.2}_{-0.3}$ | $> 475$                                       | –                | –                                  |
| 55777        | 3.56770 | -30.37909 | 5.9920 | wfss | $3.6^{+0.2}_{-0.2}$  | $9.3^{+0.1}_{-0.1}$ | $1.1^{+0.1}_{-0.1}$      | $-0.7^{+0.2}_{-0.3}$ | –   | –                | –                                  |
| 78798        | 3.49097 | -30.32492 | 5.9970 | msa  | $1.3^{+0.1}_{-0.1}$  | $8.6^{+0.1}_{-0.1}$ | $0.1^{+0.4}_{-0.4}$      | $-1.1^{+0.3}_{-0.3}$ | $> 341$                                       | –                | $> 0.7$                            |

NOTE— Measurements are corrected for magnification (Sec. 2). †: weak emission line galaxies, wELGs (Sec. 4.1).



**Figure 9.** Spectra of weak emission line galaxies (wELGs; Sec. 4.1). The figure format is the same as in Fig. 6.

#### ACKNOWLEDGEMENTS

We acknowledge the teams of the JWST observation programs, IDs 1324, 2561, 2756, 2883, 3073, 3516, 3538, 3990, and 4110 for their dedicated work in designing and planning these programs and for generously making their data publicly available. We thank Seunghwan Lim for kindly sharing their halo mass trajectories from the FLAMINGO simulation. TM would like to thank Ranga-Ram Chary for his encouraging and insightful comments on the manuscript. This work is based on observations made with the NASA/ESA/CSA *James Webb Space Telescope (JWST)*. The JWST data presented in this article were obtained from the Mikulski Archive for Space Telescopes (MAST) at the Space Telescope Science Institute. The specific observations analyzed are associated with program JWST-GO-3073 and can be accessed via DOI. We acknowledge financial support by the PRIN 2022 MUR project 2022CB3PJ3

– First Light And Galaxy aSsembly (FLAGS) funded by the European Union – Next Generation EU, and by INAF Mini-grant “Reionization and Fundamental Cosmology with High-Redshift Galaxies.” This research is supported in part by the Australian Research Council Centre of Excellence for All Sky Astrophysics in 3 Dimensions (ASTRO 3D), through project number CE170100013. We also acknowledge support from the INAF Large Grant 2022 “Extragalactic Surveys with JWST” (PI Pentericci). B.V. is supported by the European Union – NextGenerationEU RFF M4C2 1.1 PRIN 2022 project 2022ZSL4BL INSIGHT. Z.L. is supported by the KAKENHI Grant Number 24KJ0394 through the Japan Society for the Promotion of Science (JSPS).

*Software:* Astropy (Astropy Collaboration et al. 2013, 2018, 2022), bbpn (Morishita 2023), EAzY (Brammer et al. 2008), EMCEE (Foreman-Mackey et al. 2013), gsf (Morishita et al. 2019), numpy (Harris et al. 2020), python-fsps (Foreman-Mackey et al. 2014).

## REFERENCES

- Alberts, S., Williams, C. C., Helton, J. M., et al. 2023, arXiv e-prints, arXiv:2312.12207, doi: [10.48550/arXiv.2312.12207](https://doi.org/10.48550/arXiv.2312.12207)
- Arribas, S., Perna, M., Rodríguez Del Pino, B., et al. 2023, arXiv e-prints, arXiv:2312.00899, doi: [10.48550/arXiv.2312.00899](https://doi.org/10.48550/arXiv.2312.00899)
- Astropy Collaboration, Robitaille, T. P., Tollerud, E. J., et al. 2013, *A&A*, 558, A33, doi: [10.1051/0004-6361/201322068](https://doi.org/10.1051/0004-6361/201322068)
- Astropy Collaboration, Price-Whelan, A. M., Sipőcz, B. M., et al. 2018, *AJ*, 156, 123, doi: [10.3847/1538-3881/aabc4f](https://doi.org/10.3847/1538-3881/aabc4f)
- Astropy Collaboration, Price-Whelan, A. M., Lim, P. L., et al. 2022, *ApJ*, 935, 167, doi: [10.3847/1538-4357/ac7c74](https://doi.org/10.3847/1538-4357/ac7c74)
- Balogh, M. L., Morris, S. L., Yee, H. K. C., Carlberg, R. G., & Ellingson, E. 1999, *ApJ*, 527, 54, doi: [10.1086/308056](https://doi.org/10.1086/308056)
- Behroozi, P., Wechsler, R. H., Hearin, A. P., & Conroy, C. 2019, *MNRAS*, 488, 3143, doi: [10.1093/mnras/stz1182](https://doi.org/10.1093/mnras/stz1182)
- Behroozi, P. S., Wechsler, R. H., & Wu, H.-Y. 2013, *ApJ*, 762, 109, doi: [10.1088/0004-637X/762/2/109](https://doi.org/10.1088/0004-637X/762/2/109)
- Bergamini, P., Acebron, A., Grillo, C., et al. 2023a, *A&A*, 670, A60, doi: [10.1051/0004-6361/202244575](https://doi.org/10.1051/0004-6361/202244575)
- . 2023b, *ApJ*, 952, 84, doi: [10.3847/1538-4357/acd643](https://doi.org/10.3847/1538-4357/acd643)
- Bertin, E., & Arnouts, S. 1996, *A&AS*, 117, 393
- Bezanson, R., Labbe, I., Whitaker, K. E., et al. 2022, arXiv e-prints, arXiv:2212.04026, <https://arxiv.org/abs/2212.04026>
- Bocquet, S., Dietrich, J. P., Schrabback, T., et al. 2018, arXiv e-prints, arXiv:1812.01679, doi: [10.48550/arXiv.1812.01679](https://doi.org/10.48550/arXiv.1812.01679)
- Bouwens, R. J., Oesch, P. A., Stefanon, M., et al. 2021, *AJ*, 162, 47, doi: [10.3847/1538-3881/abf83e](https://doi.org/10.3847/1538-3881/abf83e)
- Brammer, G. B., van Dokkum, P. G., & Coppi, P. 2008, *ApJ*, 686, 1503, doi: [10.1086/591786](https://doi.org/10.1086/591786)
- Cai, Z., Fan, X., Bian, F., et al. 2017, *ApJ*, 839, 131, doi: [10.3847/1538-4357/aa6a1a](https://doi.org/10.3847/1538-4357/aa6a1a)
- Capak, P. L., Riechers, D., Scoville, N. Z., et al. 2011, *Nature*, 470, 233, doi: [10.1038/nature09681](https://doi.org/10.1038/nature09681)
- Cappellari, M., Emsellem, E., Krajnović, D., et al. 2011, *MNRAS*, 416, 1680, doi: [10.1111/j.1365-2966.2011.18600.x](https://doi.org/10.1111/j.1365-2966.2011.18600.x)
- Carnall, A. C., McLure, R. J., Dunlop, J. S., et al. 2023, *Nature*, 619, 716, doi: [10.1038/s41586-023-06158-6](https://doi.org/10.1038/s41586-023-06158-6)
- Casey, C. M. 2016, *ApJ*, 824, 36, doi: [10.3847/0004-637X/824/1/36](https://doi.org/10.3847/0004-637X/824/1/36)
- Casey, C. M., Cooray, A., Capak, P., et al. 2015, *ApJL*, 808, L33, doi: [10.1088/2041-8205/808/2/L33](https://doi.org/10.1088/2041-8205/808/2/L33)
- Castellano, M., Pentericci, L., Vanzella, E., et al. 2018, *ApJL*, 863, L3, doi: [10.3847/2041-8213/aad59b](https://doi.org/10.3847/2041-8213/aad59b)
- Castellano, M., Fontana, A., Treu, T., et al. 2023, *ApJL*, 948, L14, doi: [10.3847/2041-8213/accea5](https://doi.org/10.3847/2041-8213/accea5)
- Castellano, M., Napolitano, L., Fontana, A., et al. 2024, arXiv e-prints, arXiv:2403.10238, doi: [10.48550/arXiv.2403.10238](https://doi.org/10.48550/arXiv.2403.10238)
- Chabrier, G. 2003, *PASP*, 115, 763, doi: [10.1086/376392](https://doi.org/10.1086/376392)
- Chanchaiworawit, K., Guzmán, R., Salvador-Solé, E., et al. 2019, *ApJ*, 877, 51, doi: [10.3847/1538-4357/ab1a34](https://doi.org/10.3847/1538-4357/ab1a34)
- Chen, W., Kelly, P. L., Treu, T., et al. 2022, *ApJL*, 940, L54, doi: [10.3847/2041-8213/ac9585](https://doi.org/10.3847/2041-8213/ac9585)
- Chen, Z., Stark, D. P., Mason, C., et al. 2024, *MNRAS*, 528, 7052, doi: [10.1093/mnras/stae455](https://doi.org/10.1093/mnras/stae455)
- Cid Fernandes, R., Stasińska, G., Schlickmann, M. S., et al. 2010, *MNRAS*, 403, 1036, doi: [10.1111/j.1365-2966.2009.16185.x](https://doi.org/10.1111/j.1365-2966.2009.16185.x)
- Conroy, C., Gunn, J. E., & White, M. 2009, *ApJ*, 699, 486, doi: [10.1088/0004-637X/699/1/486](https://doi.org/10.1088/0004-637X/699/1/486)
- Cooper, M. C., Newman, J. A., Weiner, B. J., et al. 2008, *MNRAS*, 383, 1058, doi: [10.1111/j.1365-2966.2007.12613.x](https://doi.org/10.1111/j.1365-2966.2007.12613.x)
- Cucciati, O., Zamorani, G., Lemaux, B. C., et al. 2014, *A&A*, 570, A16, doi: [10.1051/0004-6361/201423811](https://doi.org/10.1051/0004-6361/201423811)
- Daddi, E., Delvecchio, I., Dimauro, P., et al. 2022, *A&A*, 661, L7, doi: [10.1051/0004-6361/202243574](https://doi.org/10.1051/0004-6361/202243574)
- D’Amato, Q., Gilli, R., Prandoni, I., et al. 2020, *A&A*, 641, L6, doi: [10.1051/0004-6361/202038711](https://doi.org/10.1051/0004-6361/202038711)
- Dannerbauer, H., Lehnert, M. D., Emonts, B., et al. 2017, *A&A*, 608, A48, doi: [10.1051/0004-6361/201730449](https://doi.org/10.1051/0004-6361/201730449)
- de Graaff, A., Setton, D. J., Brammer, G., et al. 2024, arXiv e-prints, arXiv:2404.05683, doi: [10.48550/arXiv.2404.05683](https://doi.org/10.48550/arXiv.2404.05683)
- Dekel, A., & Birnboim, Y. 2006, *MNRAS*, 368, 2, doi: [10.1111/j.1365-2966.2006.10145.x](https://doi.org/10.1111/j.1365-2966.2006.10145.x)
- Di Matteo, T., Springel, V., & Hernquist, L. 2005, *Nature*, 433, 604, doi: [10.1038/nature03335](https://doi.org/10.1038/nature03335)
- Dome, T., Tacchella, S., Fialkov, A., et al. 2024, *MNRAS*, 527, 2139, doi: [10.1093/mnras/stad3239](https://doi.org/10.1093/mnras/stad3239)
- Dressler, A. 1980, *ApJ*, 236, 351, doi: [10.1086/157753](https://doi.org/10.1086/157753)
- Dressler, A., & Gunn, J. E. 1983, *ApJ*, 270, 7, doi: [10.1086/161093](https://doi.org/10.1086/161093)
- Dressler, A., Smail, I., Poggianti, B. M., et al. 1999, *ApJS*, 122, 51, doi: [10.1086/313213](https://doi.org/10.1086/313213)
- Dressler, A., Oemler, Augustus, J., Couch, W. J., et al. 1997, *ApJ*, 490, 577, doi: [10.1086/304890](https://doi.org/10.1086/304890)
- Elbaz, D., Daddi, E., Le Borgne, D., et al. 2007, *A&A*, 468, 33, doi: [10.1051/0004-6361:20077525](https://doi.org/10.1051/0004-6361:20077525)
- Faisst, A. L., & Morishita, T. 2024, arXiv e-prints, arXiv:2402.13316, doi: [10.48550/arXiv.2402.13316](https://doi.org/10.48550/arXiv.2402.13316)

- Finner, K., Jee, M. J., Cho, H., et al. 2024, arXiv e-prints, arXiv:2407.02557, doi: [10.48550/arXiv.2407.02557](https://doi.org/10.48550/arXiv.2407.02557)
- Foreman-Mackey, D., Hogg, D. W., Lang, D., & Goodman, J. 2013, *PASP*, 125, 306, doi: [10.1086/670067](https://doi.org/10.1086/670067)
- Foreman-Mackey, D., Sick, J., & Johnson, B. 2014, doi: [10.5281/zenodo.12157](https://doi.org/10.5281/zenodo.12157)
- Fukugita, M., Ichikawa, T., Gunn, J. E., et al. 1996, *AJ*, 111, 1748, doi: [10.1086/117915](https://doi.org/10.1086/117915)
- Furtak, L. J., Zitrin, A., Plat, A., et al. 2023, *ApJ*, 952, 142, doi: [10.3847/1538-4357/acdc9d](https://doi.org/10.3847/1538-4357/acdc9d)
- Gatica, C., Demarco, R., Dole, H., et al. 2024, *MNRAS*, 527, 3006, doi: [10.1093/mnras/stad3404](https://doi.org/10.1093/mnras/stad3404)
- Greene, J. E., Labbe, I., Goulding, A. D., et al. 2024, *ApJ*, 964, 39, doi: [10.3847/1538-4357/ad1e5f](https://doi.org/10.3847/1538-4357/ad1e5f)
- Harikane, Y., Ouchi, M., Ono, Y., et al. 2019, *ApJ*, 883, 142, doi: [10.3847/1538-4357/ab2cd5](https://doi.org/10.3847/1538-4357/ab2cd5)
- Harikane, Y., Zhang, Y., Nakajima, K., et al. 2023, arXiv e-prints, arXiv:2303.11946, doi: [10.48550/arXiv.2303.11946](https://doi.org/10.48550/arXiv.2303.11946)
- Harris, C. R., Millman, K. J., van der Walt, S. J., et al. 2020, *Nature*, 585, 357, doi: [10.1038/s41586-020-2649-2](https://doi.org/10.1038/s41586-020-2649-2)
- Hashimoto, T., Álvarez-Márquez, J., Fudamoto, Y., et al. 2023, *ApJL*, 955, L2, doi: [10.3847/2041-8213/acf57c](https://doi.org/10.3847/2041-8213/acf57c)
- Hayashi, M., Kodama, T., Tanaka, I., et al. 2016, *ApJL*, 826, L28, doi: [10.3847/2041-8205/826/2/L28](https://doi.org/10.3847/2041-8205/826/2/L28)
- Helton, J. M., Sun, F., Woodrum, C., et al. 2023, arXiv e-prints, arXiv:2311.04270, doi: [10.48550/arXiv.2311.04270](https://doi.org/10.48550/arXiv.2311.04270)
- . 2024, *ApJ*, 962, 124, doi: [10.3847/1538-4357/ad0da7](https://doi.org/10.3847/1538-4357/ad0da7)
- Herard-Demanche, T., Bouwens, R. J., Oesch, P. A., et al. 2023, arXiv e-prints, arXiv:2309.04525, doi: [10.48550/arXiv.2309.04525](https://doi.org/10.48550/arXiv.2309.04525)
- Higuchi, R., Ouchi, M., Ono, Y., et al. 2019, *ApJ*, 879, 28, doi: [10.3847/1538-4357/ab2192](https://doi.org/10.3847/1538-4357/ab2192)
- Hopkins, P. F., Hernquist, L., Cox, T. J., et al. 2006, *ApJS*, 163, 1, doi: [10.1086/499298](https://doi.org/10.1086/499298)
- Hu, W., Wang, J., Infante, L., et al. 2021, *Nature Astronomy*, 5, 485, doi: [10.1038/s41550-020-01291-y](https://doi.org/10.1038/s41550-020-01291-y)
- Izumi, T., Matsuoka, Y., Fujimoto, S., et al. 2021, *ApJ*, 914, 36, doi: [10.3847/1538-4357/abf6dc](https://doi.org/10.3847/1538-4357/abf6dc)
- Jin, S., Sillassen, N. B., Magdis, G. E., et al. 2024, *A&A*, 683, L4, doi: [10.1051/0004-6361/202348540](https://doi.org/10.1051/0004-6361/202348540)
- Juneau, S., Bournaud, F., Charlot, S., et al. 2014, *ApJ*, 788, 88, doi: [10.1088/0004-637X/788/1/88](https://doi.org/10.1088/0004-637X/788/1/88)
- Kakimoto, T., Tanaka, M., Onodera, M., et al. 2024, *ApJ*, 963, 49, doi: [10.3847/1538-4357/ad1ff1](https://doi.org/10.3847/1538-4357/ad1ff1)
- Kashino, D., Lilly, S. J., Matthee, J., et al. 2023, *ApJ*, 950, 66, doi: [10.3847/1538-4357/acc588](https://doi.org/10.3847/1538-4357/acc588)
- Kauffmann, G., Heckman, T. M., White, S. D. M., et al. 2003, *MNRAS*, 341, 54, doi: [10.1046/j.1365-8711.2003.06292.x](https://doi.org/10.1046/j.1365-8711.2003.06292.x)
- Kelly, P. L., Diego, J. M., Rodney, S., et al. 2018, *Nature Astronomy*, 2, 334, doi: [10.1038/s41550-018-0430-3](https://doi.org/10.1038/s41550-018-0430-3)
- Kennicutt, Robert C., J. 1998, *ARA&A*, 36, 189, doi: [10.1146/annurev.astro.36.1.189](https://doi.org/10.1146/annurev.astro.36.1.189)
- Kim, S., Stiavelli, M., Trenti, M., et al. 2009, *ApJ*, 695, 809, doi: [10.1088/0004-637X/695/2/809](https://doi.org/10.1088/0004-637X/695/2/809)
- Kocevski, D. D., Onoue, M., Inayoshi, K., et al. 2023, arXiv e-prints, arXiv:2302.00012, doi: [10.48550/arXiv.2302.00012](https://doi.org/10.48550/arXiv.2302.00012)
- Kodama, T., Tanaka, I., Kajisawa, M., et al. 2007, *MNRAS*, 377, 1717, doi: [10.1111/j.1365-2966.2007.11739.x](https://doi.org/10.1111/j.1365-2966.2007.11739.x)
- Koudmani, S., Henden, N. A., & Sijacki, D. 2021, *MNRAS*, 503, 3568, doi: [10.1093/mnras/stab677](https://doi.org/10.1093/mnras/stab677)
- Koyama, Y., Polletta, M. d. C., Tanaka, I., et al. 2021, *MNRAS*, 503, L1, doi: [10.1093/mnras/slabb013](https://doi.org/10.1093/mnras/slabb013)
- Laishram, R., Kodama, T., Morishita, T., et al. 2024, *ApJL*, 964, L33, doi: [10.3847/2041-8213/ad3238](https://doi.org/10.3847/2041-8213/ad3238)
- Laporte, N., Zitrin, A., Dole, H., et al. 2022, *A&A*, 667, L3, doi: [10.1051/0004-6361/202244719](https://doi.org/10.1051/0004-6361/202244719)
- Lemaux, B. C., Le Fèvre, O., Cucciati, O., et al. 2018, *A&A*, 615, A77, doi: [10.1051/0004-6361/201730870](https://doi.org/10.1051/0004-6361/201730870)
- Li, Q., Conselice, C. J., Sarron, F., et al. 2024, arXiv e-prints, arXiv:2405.17359, doi: [10.48550/arXiv.2405.17359](https://doi.org/10.48550/arXiv.2405.17359)
- Lim, S., Tacchella, S., Schaye, J., et al. 2024, *MNRAS*, 532, 4551, doi: [10.1093/mnras/stae1790](https://doi.org/10.1093/mnras/stae1790)
- Liu, Z., Morishita, T., & Kodama, T. 2024, arXiv e-prints, arXiv:2406.11188, doi: [10.48550/arXiv.2406.11188](https://doi.org/10.48550/arXiv.2406.11188)
- Looser, T. J., D'Eugenio, F., Maiolino, R., et al. 2023, arXiv e-prints, arXiv:2306.02470, doi: [10.48550/arXiv.2306.02470](https://doi.org/10.48550/arXiv.2306.02470)
- Lotz, J. M., Koekemoer, A., Coe, D., et al. 2017, *ApJ*, 837, 97, doi: [10.3847/1538-4357/837/1/97](https://doi.org/10.3847/1538-4357/837/1/97)
- Macuga, M., Martini, P., Miller, E. D., et al. 2019, *ApJ*, 874, 54, doi: [10.3847/1538-4357/ab0746](https://doi.org/10.3847/1538-4357/ab0746)
- Madau, P., & Dickinson, M. 2014, *ARA&A*, 52, 415, doi: [10.1146/annurev-astro-081811-125615](https://doi.org/10.1146/annurev-astro-081811-125615)
- Maiolino, R., Scholtz, J., Curtis-Lake, E., et al. 2023, arXiv e-prints, arXiv:2308.01230, doi: [10.48550/arXiv.2308.01230](https://doi.org/10.48550/arXiv.2308.01230)
- Malkan, M. A., Jensen, L. D., Rodriguez, D. R., Spinoglio, L., & Rush, B. 2017, *ApJ*, 846, 102, doi: [10.3847/1538-4357/aa8302](https://doi.org/10.3847/1538-4357/aa8302)
- Mason, C. A., Trenti, M., & Treu, T. 2022, arXiv e-prints, arXiv:2207.14808. <https://arxiv.org/abs/2207.14808>

- Matthee, J., Naidu, R. P., Brammer, G., et al. 2023, arXiv e-prints, arXiv:2306.05448, doi: [10.48550/arXiv.2306.05448](https://doi.org/10.48550/arXiv.2306.05448)
- Merlin, E., Bonchi, A., Paris, D., et al. 2022, *ApJL*, 938, L14, doi: [10.3847/2041-8213/ac8f93](https://doi.org/10.3847/2041-8213/ac8f93)
- Miller, T. B., Chapman, S. C., Aravena, M., et al. 2018, *Nature*, 556, 469, doi: [10.1038/s41586-018-0025-2](https://doi.org/10.1038/s41586-018-0025-2)
- Morishita, T. 2023, mtakahiro/bbnp: v1.3, v1.3, Zenodo, doi: [10.5281/zenodo.10067906](https://doi.org/10.5281/zenodo.10067906)
- Morishita, T., & Stiavelli, M. 2023, *ApJL*, 946, L35, doi: [10.3847/2041-8213/acbf50](https://doi.org/10.3847/2041-8213/acbf50)
- Morishita, T., Abramson, L. E., Treu, T., et al. 2019, *ApJ*, 877, 141, doi: [10.3847/1538-4357/ab1d53](https://doi.org/10.3847/1538-4357/ab1d53)
- Morishita, T., Roberts-Borsani, G., Treu, T., et al. 2023, *ApJL*, 947, L24, doi: [10.3847/2041-8213/acb99e](https://doi.org/10.3847/2041-8213/acb99e)
- Morishita, T., Stiavelli, M., Chary, R.-R., et al. 2024, *ApJ*, 963, 9, doi: [10.3847/1538-4357/ad1404](https://doi.org/10.3847/1538-4357/ad1404)
- Newman, A. B., Belli, S., & Ellis, R. S. 2015, *ApJL*, 813, L7, doi: [10.1088/2041-8205/813/1/L7](https://doi.org/10.1088/2041-8205/813/1/L7)
- Noble, A. G., McDonald, M., Muzzin, A., et al. 2017, *ApJL*, 842, L21, doi: [10.3847/2041-8213/aa77f3](https://doi.org/10.3847/2041-8213/aa77f3)
- Oke, J. B., & Gunn, J. E. 1983, *ApJ*, 266, 713, doi: [10.1086/160817](https://doi.org/10.1086/160817)
- Oteo, I., Ivison, R. J., Dunne, L., et al. 2018, *ApJ*, 856, 72, doi: [10.3847/1538-4357/aaaf1f](https://doi.org/10.3847/1538-4357/aaaf1f)
- Overzier, R. A. 2016, *A&A Rv*, 24, 14, doi: [10.1007/s00159-016-0100-3](https://doi.org/10.1007/s00159-016-0100-3)
- Paccagnella, A., Vulcani, B., Poggianti, B. M., et al. 2019, *MNRAS*, 482, 881, doi: [10.1093/mnras/sty2728](https://doi.org/10.1093/mnras/sty2728)
- . 2017, *ApJ*, 838, 148, doi: [10.3847/1538-4357/aa64d7](https://doi.org/10.3847/1538-4357/aa64d7)
- Paris, D., Merlin, E., Fontana, A., et al. 2023, arXiv e-prints, arXiv:2301.02179, doi: [10.48550/arXiv.2301.02179](https://doi.org/10.48550/arXiv.2301.02179)
- Peng, C. Y., Ho, L. C., Impey, C. D., & Rix, H.-W. 2010, *AJ*, 139, 2097, doi: [10.1088/0004-6256/139/6/2097](https://doi.org/10.1088/0004-6256/139/6/2097)
- Pensabene, A., Cantalupo, S., Cicone, C., et al. 2024, *A&A*, 684, A119, doi: [10.1051/0004-6361/202348659](https://doi.org/10.1051/0004-6361/202348659)
- Pérez-Martínez, J. M., Kodama, T., Koyama, Y., et al. 2024, *MNRAS*, 527, 10221, doi: [10.1093/mnras/stad3805](https://doi.org/10.1093/mnras/stad3805)
- Poggianti, B. M., Aragón-Salamanca, A., Zaritsky, D., et al. 2009, *ApJ*, 693, 112, doi: [10.1088/0004-637X/693/1/112](https://doi.org/10.1088/0004-637X/693/1/112)
- Polletta, M., Soucail, G., Dole, H., et al. 2021, *A&A*, 654, A121, doi: [10.1051/0004-6361/202140612](https://doi.org/10.1051/0004-6361/202140612)
- Postman, M., Coe, D., Benítez, N., et al. 2012, *ApJS*, 199, 25, doi: [10.1088/0067-0049/199/2/25](https://doi.org/10.1088/0067-0049/199/2/25)
- Roberts-Borsani, G., Treu, T., Shapley, A., et al. 2024, arXiv e-prints, arXiv:2403.07103, doi: [10.48550/arXiv.2403.07103](https://doi.org/10.48550/arXiv.2403.07103)
- Sanders, R. L., Shapley, A. E., Topping, M. W., Reddy, N. A., & Brammer, G. B. 2023, arXiv e-prints, arXiv:2303.08149, doi: [10.48550/arXiv.2303.08149](https://doi.org/10.48550/arXiv.2303.08149)
- Shimakawa, R., Kodama, T., Hayashi, M., et al. 2018, *MNRAS*, 473, 1977, doi: [10.1093/mnras/stx2494](https://doi.org/10.1093/mnras/stx2494)
- Somerville, R. S., Barden, M., Rix, H.-W., et al. 2008, *ApJ*, 672, 776, doi: [10.1086/523661](https://doi.org/10.1086/523661)
- Steidel, C. C., Adelberger, K. L., Dickinson, M., et al. 1998, *ApJ*, 492, 428, doi: [10.1086/305073](https://doi.org/10.1086/305073)
- Steidel, C. C., Adelberger, K. L., Shapley, A. E., et al. 2005, *ApJ*, 626, 44, doi: [10.1086/429989](https://doi.org/10.1086/429989)
- . 2000, *ApJ*, 532, 170, doi: [10.1086/308568](https://doi.org/10.1086/308568)
- Steinhardt, C. L., Jauzac, M., Acebron, A., et al. 2020, *ApJS*, 247, 64, doi: [10.3847/1538-4365/ab75ed](https://doi.org/10.3847/1538-4365/ab75ed)
- Stiavelli, M. 2005, Searching for galaxies at  $z \gtrsim 6.5$  in the Hubble Ultra Deep Field, HST Proposal ID 10632. Cycle 14
- Strait, V., Brammer, G., Muzzin, A., et al. 2023, *ApJL*, 949, L23, doi: [10.3847/2041-8213/acd457](https://doi.org/10.3847/2041-8213/acd457)
- Suess, K. A., Weaver, J. R., Price, S. H., et al. 2024, arXiv e-prints, arXiv:2404.13132, doi: [10.48550/arXiv.2404.13132](https://doi.org/10.48550/arXiv.2404.13132)
- Sun, F., Egami, E., Pirzkal, N., et al. 2023, *ApJ*, 953, 53, doi: [10.3847/1538-4357/acd53c](https://doi.org/10.3847/1538-4357/acd53c)
- Tanaka, M., Onodera, M., Shimakawa, R., et al. 2024, *ApJ*, 970, 59, doi: [10.3847/1538-4357/ad5316](https://doi.org/10.3847/1538-4357/ad5316)
- Tarrío, P., Melin, J. B., & Arnaud, M. 2019, *A&A*, 626, A7, doi: [10.1051/0004-6361/201834979](https://doi.org/10.1051/0004-6361/201834979)
- Thomas, D., Maraston, C., Bender, R., & Mendes de Oliveira, C. 2005, *ApJ*, 621, 673, doi: [10.1086/426932](https://doi.org/10.1086/426932)
- Toshikawa, J., Kashikawa, N., Overzier, R., et al. 2014, *ApJ*, 792, 15, doi: [10.1088/0004-637X/792/1/15](https://doi.org/10.1088/0004-637X/792/1/15)
- Toshikawa, J., Wuyts, S., Kashikawa, N., et al. 2024, *MNRAS*, 527, 6276, doi: [10.1093/mnras/stad3162](https://doi.org/10.1093/mnras/stad3162)
- Treu, T., Ellis, R. S., Kneib, J.-P., et al. 2003, *ApJ*, 591, 53, doi: [10.1086/375314](https://doi.org/10.1086/375314)
- Treu, T., Roberts-Borsani, G., Bradac, M., et al. 2022, *ApJ*, 935, 110, doi: [10.3847/1538-4357/ac8158](https://doi.org/10.3847/1538-4357/ac8158)
- Übler, H., Maiolino, R., Curtis-Lake, E., et al. 2023, *A&A*, 677, A145, doi: [10.1051/0004-6361/202346137](https://doi.org/10.1051/0004-6361/202346137)
- Umehata, H., Smail, I., Steidel, C. C., et al. 2021, *ApJ*, 918, 69, doi: [10.3847/1538-4357/ac1106](https://doi.org/10.3847/1538-4357/ac1106)
- Venemans, B. P., Röttgering, H. J. A., Miley, G. K., et al. 2007, *A&A*, 461, 823, doi: [10.1051/0004-6361:20053941](https://doi.org/10.1051/0004-6361:20053941)
- Vulcani, B., Fritz, J., Poggianti, B. M., et al. 2020, *ApJ*, 892, 146, doi: [10.3847/1538-4357/ab7bdd](https://doi.org/10.3847/1538-4357/ab7bdd)
- Wang, T., Elbaz, D., Daddi, E., et al. 2016, *ApJ*, 828, 56, doi: [10.3847/0004-637X/828/1/56](https://doi.org/10.3847/0004-637X/828/1/56)
- Werle, A., Poggianti, B., Moretti, A., et al. 2022, *ApJ*, 930, 43, doi: [10.3847/1538-4357/ac5f06](https://doi.org/10.3847/1538-4357/ac5f06)



Wetzel, A. R., Tinker, J. L., & Conroy, C. 2012, MNRAS,  
424, 232, doi: [10.1111/j.1365-2966.2012.21188.x](https://doi.org/10.1111/j.1365-2966.2012.21188.x)

Witten, C., McClymont, W., Laporte, N., et al. 2024, arXiv  
e-prints, arXiv:2407.07937,  
doi: [10.48550/arXiv.2407.07937](https://doi.org/10.48550/arXiv.2407.07937)